

Anisotropy and temperature dependence of the optical conductivity in LaMnO_3

K. H. Ahn* and A. J. Millis

*Department of Physics and Astronomy, Rutgers University
Piscataway, New Jersey 08854*

Abstract

A tight binding parameterization of the band structure, along with a mean field treatment of Hund, electron-electron, and electron-lattice couplings, is used to obtain the full optical conductivity tensor of LaMnO_3 as a function of temperature. We predict striking changes with temperature in the functional form and magnitude of the optical absorption. Comparison of our results to data will determine the Hund, electron-lattice, and electron-electron interactions.

78.20.Bh, 78.20.-e, 71.20.Be, 72.15.Gd

I. INTRODUCTION

In recent years the colossal magnetoresistance manganese perovskites have attracted much attention.¹ The low energy ($\hbar\omega < 4$ eV) physics of these materials is believed to be governed by Mn e_g electrons, which are coupled by a strong Hund's coupling, J_H , to Mn t_{2g} symmetry 'core spins' and also interact with each other and with lattice distortions. Three important and still unresolved issues are the value of J_H , the strength of the Jahn-Teller(JT) electron-phonon coupling λ , and the magnitude of the effective e_g - e_g on-site Coulomb interaction U governing the low energy physics. The relative importance of the electron-electron and electron-phonon interactions is a particularly important open question.

Hund's coupling J_H is believed to be large, because in good samples at low temperatures, observed magnetic moments are close to their saturation values.² However, J_H has not been directly measured. Estimates ranging from $2J_H S_c \approx 2$ eV (Ref. 3) to 3 eV (Ref. 4) have been obtained from the analysis of the optical measurements of doped materials. However, these estimates depend upon proper identification of features in the observed optical conductivity, and this identification is at present disputed.

The value of the effective Coulomb repulsion is also unclear. High energy photoemission spectroscopy⁵ yields a bare repulsion $U_{\text{bare}} \approx 8$ eV, but also implies that the manganites are in the class of charge-transfer materials,⁶ as are the high- T_c cuprates. In charge-transfer materials the low energy ($\hbar\omega \ll U_{\text{bare}}$) electronic degrees of freedom are complicated linear combinations of transition metal and oxygen orbitals, and the effective repulsion for these orbitals may be much less than U_{bare} . For example, in high T_c materials, $U_{\text{bare}} \approx 10$ eV but the U relevant to the low energy physics is rather less; perhaps $U \approx 2$ eV (Ref. 7). The proper value of the U relevant to the low energy ($\hbar\omega < 4$ eV) physics of manganites is at present disputed. Some authors argue that electron-electron interactions are dominant; others that electron-phonon interactions are crucial.

In this communication, we show how measurements of the magnitude, anisotropy and temperature dependence of the optical conductivity of the manganites' insulating 'parent compound' LaMnO_3 can help to resolve these issues. We obtain an effective Hamiltonian for the low energy degrees of freedom by fitting band theory calculations to a tight binding model and adding Coulomb interaction terms. We then determine its optical conductivity as a function of temperature, and show how the different features in the spectrum may be used to determine the interaction parameters. The advantage of the tight binding approach is that it compactly represents the low energy degrees of freedom, allows straightforward inclusion of interaction effects, and is computationally cheap enough that many parameter choices may be investigated.

The material is a $(0,0,\pi)$ antiferromagnet at low temperatures, while a paramagnet at room temperature. The Hund's coupling therefore leads to a peak structure with a pronounced and strongly temperature-dependent anisotropy. Observation of this effect would provide a definitive determination of the Hund's coupling parameter.

The Jahn-Teller and Coulomb interactions lead to similar effects in the absorption spectrum; indeed the two interactions roughly add. The strength of the Jahn-Teller coupling may be determined from crystallography data or from band theory; interestingly the two determinations agree very well. The effect of the Jahn-Teller coupling on the optical conductivity may essentially be calculated exactly. We compare the results of this calculation to

the optical conductivity data, and argue that differences are due to the Coulomb interaction. To estimate the strength of the Coulomb interaction we use a Hartree-Fock approximation and calculate the optical conductivity of the Jahn-Teller plus Coulomb system. The optical conductivity of LaMnO_3 was previously calculated by Solovyev *et al.*⁸ and by Terakura *et al.*⁹ using the LDA method, but they did not consider the temperature dependence, or present information about the dependence of the observed conductivity on parameters. When we calculate using parameters tuned to give similar band gaps, we find the maximum conductivity is factor of 2-3 larger than the result in Ref. 8 and 4 times than in Ref. 9. The difference in absorption strength is not understood at present, but is discussed in more detail in Section V, which shows that the error is unlikely to arise from the tight binding approach.

The rest of this paper is organized as follows: Section II presents the Hamiltonian, band structure, and the parameter determination, Section III gives the formulation of the optical conductivity, calculation results, and the comparison with experiments, Section IV describes the effect of the Coulomb interaction, Section V discusses the accuracy of the approximation we have used, and Section VI is the conclusion.

II. HAMILTONIAN AND BAND STRUCTURE

At and below room temperature, LaMnO_3 exists in a distorted form of the ABO_3 perovskite structure. According to band theory calculations^{10–12} the conduction band is derived mainly from Mn e_g symmetry d-orbitals and is well separated from other bands. We find that the band structure appropriate to the ideal cubic ABO_3 perovskite structure may be well represented by the following tight binding model.

$$H_{\text{KE}} + H_{\mu} = -\frac{1}{2} \sum_{\vec{i}, \vec{\delta}, a, b, \alpha} t_{\vec{\delta}}^{ab} d_{i\alpha}^{\dagger} d_{\vec{i}+\vec{\delta}\alpha} + H.c. - \mu \sum_{\vec{i}, a, \alpha} d_{i\alpha}^{\dagger} d_{i\alpha}. \quad (1)$$

Here \vec{i} represents the coordinates of the Mn sites (which in the ideal structure are arranged in a simple cubic lattice), a, b represent the two degenerate Mn e_g orbitals on a site, $\delta (= \pm x, y, z)$ labels the nearest neighbors of a Mn site, α denotes the spin state, and $t_{\vec{\delta}}^{ab}$ is the hopping amplitude between orbital a on site \vec{i} and b on site $\vec{i} + \vec{\delta}$. We choose $|\psi_1\rangle = |3z^2 - r^2\rangle$ and $|\psi_2\rangle = |x^2 - y^2\rangle$ as the two linearly independent e_g orbitals on a site. The hopping matrix $t_{\vec{\delta}}^{ab}$ has a special form: for hopping along the z direction, it connects only the two $|3z^2 - r^2\rangle$ states, thus

$$t_z = t_{-z} = t_o \begin{pmatrix} 1 & 0 \\ 0 & 0 \end{pmatrix}. \quad (2)$$

The hopping matrices in the other bond directions are obtained by appropriate rotations and are

$$t_x = t_{-x} = t_o \begin{pmatrix} 1/4 & -\sqrt{3}/4 \\ -\sqrt{3}/4 & 3/4 \end{pmatrix}, \quad (3)$$

$$t_y = t_{-y} = t_o \begin{pmatrix} 1/4 & \sqrt{3}/4 \\ \sqrt{3}/4 & 3/4 \end{pmatrix}. \quad (4)$$

As noted in the introduction, there is a substantial high energy ($U_{\text{bare}} \approx 8$ eV) photoemission evidence for strong on-site Coulomb interactions in the manganites, which places them in the class of ‘charge transfer’ materials. The relevance of the band theory calculation may therefore be questioned. We argue, however, that the effects of the interactions at the low ($\hbar\omega < 4$ eV) energies of interest may be determined by comparing the predictions of the band theory calculation to data; the results we present will allow this comparison to be made. The high T_c superconductors provide an instructive example. These are also charge transfer insulators with a very large high energy on-site repulsion U_{high} (Ref. 7,13). The low energy excitations are complicated objects called Zhang-Rice singlets, but it has been established that the effective interaction relevant to the low energy theory is much less than U_{high} , and that band theory (albeit with a renormalized hopping) describes the electron dispersion well. We therefore suggest that band theory is an appropriate starting point in the manganite case as well.

We now turn to the electron-lattice coupling. Below 800 K, LaMnO_3 exists in a distorted form of the ABO_3 perovskite structure. The important distortion is a Jahn-Teller distortion in which Mn-O bond lengths are changed in such a way that if we choose a Mn site as an origin, the distortion is even-parity and the sum of the lengths of the 6 Mn-O bonds is unchanged. This distortion lifts the degeneracy of the e_g levels on a site. To represent this we define u_i^a as the displacement along the a direction of an oxygen ion located between Mn ions at \vec{i} and $\vec{i} + \hat{a}$, and we define $v_i^a = u_i^a - u_{i-\hat{a}}^a$. The Jahn-Teller distortion term may then be written as

$$H_{\text{JT}} = -\lambda \sum_{\vec{i}, \alpha} \begin{pmatrix} d_{1,\vec{i},\alpha}^\dagger \\ d_{2,\vec{i},\alpha}^\dagger \end{pmatrix}^T \begin{pmatrix} v_i^z - \frac{1}{2}(v_i^x + v_i^y) & \frac{\sqrt{3}}{2}(v_i^x - v_i^y) \\ \frac{\sqrt{3}}{2}(v_i^x - v_i^y) & -v_i^z + \frac{1}{2}(v_i^x + v_i^y) \end{pmatrix} \begin{pmatrix} d_{1,\vec{i},\alpha} \\ d_{2,\vec{i},\alpha} \end{pmatrix}. \quad (5)$$

The experimentally observed distortion has two components: a Q_2 type staggered distortion with wave vector $(\pi, \pi, 0)$, and a Q_3 type uniform distortion. This distortion leads to a Jahn-Teller term of the form

$$H_{\text{JT}} = -\lambda \sum_{\vec{i}, \alpha} \begin{pmatrix} d_{1,\vec{i},\alpha}^\dagger \\ d_{2,\vec{i},\alpha}^\dagger \end{pmatrix}^T \begin{pmatrix} -\bar{v} & (-1)^{i_x+i_y}\bar{w} \\ (-1)^{i_x+i_y}\bar{w} & \bar{v} \end{pmatrix} \begin{pmatrix} d_{1,\vec{i},\alpha} \\ d_{2,\vec{i},\alpha} \end{pmatrix}, \quad (6)$$

where \bar{w} and \bar{v} are the amplitudes of the staggered(Q_2) and uniform(Q_3) distortion respectively.

We next consider the Hund’s coupling. This leads to a term

$$H_{\text{Hund}} = \sum_{\vec{i}, a, \alpha} J_{\text{H}} \vec{S}_{\text{c}}^i \cdot d_{\vec{i}, a, \alpha}^\dagger \vec{\sigma}_{\alpha\beta} d_{\vec{i}, a, \beta}, \quad (7)$$

where \vec{S}_{c}^i represents the t_{2g} core spin and $\vec{\sigma}$ the Pauli matrix. At $T = 0$ K, the magnetic structure is of a $(0,0,\pi)$ antiferromagnet; leading to

$$H_{\text{Hund}} = J_{\text{H}} S_{\text{c}} \sum_{\vec{i}, a} \left[\left(1 - (-1)^{i_z}\right) d_{\vec{i}, a, \uparrow}^\dagger d_{\vec{i}, a, \uparrow} + \left(1 + (-1)^{i_z}\right) d_{\vec{i}, a, \downarrow}^\dagger d_{\vec{i}, a, \downarrow} \right]. \quad (8)$$

The total Hamiltonian is the sum of the terms considered so far.

$$H_{\text{tot}} = H_{\text{KE}} + H_{\mu} + H_{\text{JT}} + H_{\text{Hund}}. \quad (9)$$

Fourier transforming into k space results in the expression for H_{tot} given in the Appendix A. By diagonalizing this matrix, we can find the energy levels.

At $T = 0$ K, the unit cell is doubled twice, once by spin and once by orbital ordering. We have two orbital states for each of the two spin states, and four Mn sites per unit cell. Due to the symmetry between two spin states, we will have two-fold degeneracy for each level. Therefore, we have eight separate bands. The ground state is obtained by filling the energy levels below the chemical potential μ , which is determined to give the correct number of electrons per unit cell. We denote the energy levels by $E_j(\vec{k})$ ($j=1,2,\dots,8$) in the order of the increasing energy. The band structure determined by Eq. (9) is shown in Fig. 1 for the parameters which provide the best fit to the published band calculations.¹¹ Crudely speaking, the bands fall into 4 pairs, which may be understood by setting $t_o = 0$ (as occurs at $(\pi/2, \pi/2, \pi/2)$); in this case we have four separate energy levels on each site: which are $E_{1,2} = -\lambda\sqrt{\bar{v}^2 + \bar{w}^2}$, $E_{3,4} = \lambda\sqrt{\bar{v}^2 + \bar{w}^2}$, $E_{5,6} = 2J_{\text{H}}S_{\text{c}} - \lambda\sqrt{\bar{v}^2 + \bar{w}^2}$, and $E_{7,8} = 2J_{\text{H}}S_{\text{c}} + \lambda\sqrt{\bar{v}^2 + \bar{w}^2}$. When we have non-zero t_o , these levels split and become dispersive. In the low temperature $(0,0,\pi)$ antiferromagnetic structure, the Hund's coupling suppresses the z -directional hopping; the bands thus become more two-dimensional as $J_{\text{H}}S_{\text{c}}$ increases.

Band theory calculation is used to determine the three parameter values of our model Hamiltonian: t_o , λ , and $J_{\text{H}}S_{\text{c}}$. To find these, we fit our band structure calculation to the LDA band calculation for the JT distorted LaMnO₃ by Satpathy *et al.*¹¹ at high symmetry points in reciprocal space, $(\pi,0,0)$, $(0,0,0)$, $(\pi/2, \pi/2, \pi/2)$, and $(\pi,0,\pi/2)$. The standard deviation is ≈ 0.2 eV, and maximal error of 0.4 eV occurs at $(\pi/2, \pi/2, \pi/2)$ for the lower JT level of the upper Hund state, $E_{5,6}$. The determined parameter values are $t_o=0.622$ eV, $\lambda=1.38$ eV/Å, and $2J_{\text{H}}S_{\text{c}}=2.47$ eV. The fitted band structure is shown in Fig. 1. These parameters fit the LDA band calculations for the JT distorted and buckled actual LaMnO₃ structure published by Satpathy *et al.*¹⁰ with a similar size of error. The above t_o and $J_{\text{H}}S_{\text{c}}$ are similar to the values obtained by Myrasov *et al.*¹⁴ from an LDA calculation for the ideal cubic structure.

This parameter λ may be independently determined by fitting the observed lattice distortion¹⁵ to a simple model of localized electrons which are Jahn-Teller-coupled to a harmonic lattice as explained in Ref. 16. This reference shows that the amplitude of the observed distortion fixes the parameter $\lambda/(K_1 a_0)$, where K_1 is the spring constant between the nearest neighbor Mn-O pairs and a_0 is the average Mn-O distance. The following two equations are derived in Ref. 16.

$$a_o e^a = \frac{\lambda}{K_1 + 2K_2} [\cos 2(\theta_1 + \psi^a) + \cos 2(\theta_2 + \psi^a)] \quad (10)$$

$$u_s^a = \frac{\lambda}{2K_1} [\cos 2(\theta_1 + \psi^a) - \cos 2(\theta_2 + \psi^a)] \quad (11)$$

where e^a ($a = x, y, z$) is the uniform strain, u_s^a is the staggered oxygen displacement, K_2 is the nearest neighbor Mn-Mn spring constant, $\psi^{x,y,z} = -\pi/3, \pi/3, 0$, and θ_1, θ_2 parameterize the orbital states on the two sublattices: $|\psi\rangle = \cos\theta|3z^2 - r^2\rangle + \sin\theta|x^2 - y^2\rangle$. (Eq.

(10) corrects a factor of two error in Eq. (10) of Ref. 16.) Using the relation $\theta_2 = \pi - \theta_1$ derived in Ref. 16, we get the following expression of $\lambda/(K_1 a_0)$.

$$\frac{\lambda}{K_1 a_0} = \sqrt{\left(e^z \frac{1 + 2K_2/K_1}{2}\right)^2 + \left(\frac{2u_s^x}{\sqrt{3}a_0}\right)^2} \quad (12)$$

From Ellemans *et al.*'s results,¹⁵ $e^z = -0.0288$, $u_s^x = 0.141 \text{ \AA}$, and $a_0 = 4.034 \text{ \AA}$. For $0 \leq K_2/K_1 \leq 1.0$, we obtain $0.0428 \leq \lambda/(K_1 a_0) \leq 0.0591$. K_1 is estimated from the frequency of the highest lying bond stretching mode measured in this material by Jung *et al.*¹⁷ The measured bond stretching mode has a peak at 70.3 meV. From the relation $(\hbar\omega)^2 = 2K_1(m_{\text{Mn}}^{-1} + m_{\text{O}}^{-1})$, we obtain $K_1 = 7.36 \text{ eV/\AA}^2$. Using $a_0 = 4.034 \text{ \AA}$, the range of λ obtained is between 1.27 eV/\AA and 1.76 eV/\AA, which includes the value obtained above. We can, in fact, determine the lower bound of K_2/K_1 from the structural transition temperature as explained in Ref. 16. In Ref. 16, the mean field estimation of the structural phase transition temperature was found to be $T_s^{\text{MF}} = 3\lambda^2 K_2/[2K_1(K_1 + 2K_2)] = 750 \text{ K} = 65 \text{ meV}$. Considering that mean field theory overestimates the transition temperature, we obtain

$$\frac{3}{2} \frac{\lambda^2 K_2}{K_1(K_1 + 2K_2)} > 65 \text{ meV}. \quad (13)$$

Combining the previous expression of $\lambda/(K_1 a_0)$ versus K_2/K_1 , we can determine the range of K_2/K_1 . The determined range is $K_2/K_1 > 0.26$, and gives $\lambda > 1.36 \text{ eV/\AA}$, which is remarkably close to the value obtained by band fitting.

III. OPTICAL CONDUCTIVITY

A. At T= 0 K

Optical conductivity per volume, σ , can be found in the following way. The electromagnetic field couples to the electrons via the Peierls phase factor $t_\delta \rightarrow t_\delta \exp(i e \vec{A} \cdot \vec{\delta} a_0 / \hbar)$. This implies the total current operator

$$\hat{\vec{J}} = \frac{\delta H}{\delta \vec{A}} = -\frac{iea_0}{2\hbar} \sum_{\vec{i}, \vec{\delta}, a, b, \alpha} t_\delta^{ab} \vec{\delta} \left[\exp\left(\frac{ie \vec{A} \cdot \vec{\delta} a_0}{\hbar}\right) d_{i a \alpha}^\dagger d_{i + \vec{\delta} b \alpha} - H.c. \right]. \quad (14)$$

By expanding about \vec{A} , we obtain

$$\hat{\vec{J}} = \hat{\vec{J}}_p + \hat{\vec{J}}_d + O(A^2), \quad (15)$$

where

$$\hat{\vec{J}}_p = -\frac{iea_0}{2\hbar} \sum_{\vec{i}, \vec{\delta}, a, b, \alpha} t_\delta^{ab} \vec{\delta} \left(d_{i a \alpha}^\dagger d_{i + \vec{\delta} b \alpha} - H.c. \right), \quad (16)$$

$$\hat{\vec{J}}_d = \frac{ea_0}{2\hbar} \sum_{\vec{i}, \vec{\delta}, a, b, \alpha} t_\delta^{ab} \vec{\delta} \frac{e \vec{A} \cdot \vec{\delta} a_0}{\hbar} \left(d_{i a \alpha}^\dagger d_{i + \vec{\delta} b \alpha} + H.c. \right). \quad (17)$$

Since $\vec{J}(\vec{A}) = \langle 0(\vec{A}) | \hat{J}_p + \hat{J}_d | 0(\vec{A}) \rangle = -i\omega \Sigma \vec{A} + O(A^2)$, where $\Sigma = \int dV \sigma$ is the total conductivity, by expanding $\vec{J}(\vec{A})$ up to linear order in \vec{A} , we can find σ . Since \hat{J}_d is already linear in \vec{A} , it gives the following contribution in σ .

$$\sigma_d^{\lambda\nu} = -\frac{1}{i\omega} \left(\frac{ea_0}{\hbar} \right)^2 K_{\lambda\lambda} \delta_{\lambda\nu} \frac{1}{a_0^3} \quad (18)$$

where

$$K_{\lambda\lambda} = \frac{1}{N_{Mn}} \langle 0 | \frac{1}{2} \sum_{\vec{i}, \vec{\delta}=\pm\hat{\lambda}, a, b, \alpha} t_{\vec{\delta}}^{ab} \left(d_{i\alpha}^\dagger d_{i+\vec{\delta}b\alpha} + H.c. \right) | 0 \rangle. \quad (19)$$

Since \hat{J}_p does not contain \vec{A} , we should use higher order perturbation to obtain linear term. Second order perturbation yields

$$\sigma_p^{\lambda\nu} = -\frac{1}{i\omega N_{Mn} a_0^3} \sum_n \frac{\langle 0 | J_{p\lambda}^\dagger | n \rangle \langle n | J_{p\nu} | 0 \rangle}{\hbar\omega - (E_n - E_0) + i\epsilon}, \quad (20)$$

where ϵ is an infinitesimal introduced to make the expression well defined. The above procedure is a standard linear response theory, which is also used in Ref. 18, and explained in detail in Ref. 19.

By transforming into energy eigenbasis, we can obtain explicit expression of $K_{\lambda\lambda}$ and σ_p , which gives σ . The results are

$$K^{\lambda\lambda} = \frac{2}{(2\pi)^3} \int_R d\vec{k} \sum_{E_j(\vec{k}) < \mu} 2 \cos k_a B_a(\vec{k})_{jj} \quad (21)$$

and

$$(\sigma_p)_{aa} = -\frac{2}{i\omega a_0^3} \frac{1}{(2\pi)^3} \int_R d\vec{k} \sum_{E_j(\vec{k}) < \mu, E_{j'}(\vec{k}) > \mu} \frac{|(ea_0/\hbar) 2 \sin k_a B_a(\vec{k})_{jj'}|^2}{\hbar\omega - E_{j'}(\vec{k}) + E_j(\vec{k}) + i\epsilon}, \quad (22)$$

where

$$B_a(\vec{k}) = M(\vec{k})^\dagger T_a M(\vec{k}), \quad (23)$$

$$T_x = \begin{pmatrix} t_x & 0 & 0 & 0 \\ 0 & -t_x & 0 & 0 \\ 0 & 0 & t_x & 0 \\ 0 & 0 & 0 & -t_x \end{pmatrix}, \quad (24)$$

$$T_y = \begin{pmatrix} t_y & 0 & 0 & 0 \\ 0 & -t_y & 0 & 0 \\ 0 & 0 & t_y & 0 \\ 0 & 0 & 0 & -t_y \end{pmatrix}, \quad (25)$$

$$T_z = \begin{pmatrix} t_z & 0 & 0 & 0 \\ 0 & t_z & 0 & 0 \\ 0 & 0 & -t_z & 0 \\ 0 & 0 & 0 & -t_z \end{pmatrix}, \quad (26)$$

$M(\vec{k})$ is the matrix diagonalizing $H_{\vec{k},\uparrow}$ in the Appendix A, a_o is the distance between Mn ions, and R is defined in the Appendix A. The factor of 2 comes from the two spin states. Therefore, the real part of σ is

$$Re[\sigma_{aa}] = \frac{2}{\omega a_o^3} \frac{1}{(2\pi)^3} \int_R d\vec{k} \sum_{E_j(\vec{k}) < \mu, E_{j'}(\vec{k}) > \mu} \left| \frac{ea_o}{\hbar} 2 \sin k_a B_a(\vec{k})_{jj'} \right|^2 \frac{\epsilon}{[\hbar\omega - E_{j'}(\vec{k}) + E_j(\vec{k})]^2 + \epsilon^2}. \quad (27)$$

The total oscillator strength in the conductivity of our Hamiltonian may be obtained as follows.^{18,20} Optical conductivity σ can be written as

$$\sigma^{\lambda\nu}(\omega) = \left(\frac{e^2}{\hbar^2 a_o} K_{\lambda\nu} \delta_{\lambda\nu} - \chi_{\lambda\nu} \right) / (-i\omega), \quad (28)$$

where

$$\chi_{\lambda\nu} = \frac{1}{N_{Mn} a_o^3} \sum_n \frac{\langle 0 | J_{p\lambda}^\dagger | n \rangle \langle n | J_{p\nu} | 0 \rangle}{\hbar\omega - (E_n - E_0) + i\epsilon}. \quad (29)$$

At large ω , $\chi_{\lambda\nu} \propto 1/\omega$. Therefore, $\lim_{\omega \rightarrow \infty} \sigma^{\lambda\nu}(\omega) = \frac{e^2}{\hbar^2 a_o} K_{\lambda\lambda} \delta_{\lambda\nu} / (-i\omega)$. Large ω limit of the Kramers-Kronig relation

$$Im[\sigma(\omega)] = -(2\omega/\pi) P \int_0^\infty ds \frac{Re[\sigma(s)]}{s^2 - \omega^2} \quad (30)$$

yields the following sum rule:

$$K^{\lambda\lambda} = \frac{\hbar^2 a_o}{e^2} \frac{2}{\pi} \int_0^\infty d\omega Re[\sigma_{\lambda\lambda}(\omega)]. \quad (31)$$

From crystallography studies in Ref. 15, $\bar{w}=0.488 \text{ \AA}$ and $\bar{v}=0.174 \text{ \AA}$ at $T = 0 \text{ K}$. Figures 2(a), 2(c), and 2(e) show the $T=0 \text{ K}$ optical conductivities σ_{xx} and σ_{zz} calculated for three values of the coupling constant λ with t_o and $J_H S_c$ predicted by band theory and \bar{v} and \bar{w} from crystallographic data. Figure 2(a) shows σ_{xx} and σ_{zz} for the case $2\lambda\sqrt{\bar{v}^2 + \bar{w}^2} < 2J_H S_c$. For σ_{xx} (solid line), we see a large peak at the Jahn-Teller splitting, corresponding to motion within one plane. Note the jump in absorption at the gap edge, characteristic two-dimensional feature, a weak feature at $2J_H S_c$, corresponding to electron trajectories which overlap from one plane to the next, and an extremely weak feature at the sum of the Jahn-Teller and Hund's splitting. For σ_{zz} (dotted line), we see a very weak feature at the Jahn-Teller energy, corresponding to a small amplitude for an electron to tunnel through an intervening plane and land on a 'correctly oriented' core spin, a large peak at the Hund's energy, and another peak at the sum of Hund's and Jahn-Teller energies. The sharp peak at the Hund's energy in σ_{zz} originates from the essentially parallel bands seen in Fig. 1 between $(\pi/2, \pi/2, \pi/2)$ and $(\pi, 0, \pi/2)$. In LSDA band calculation in Ref. 11, these two bands are not exactly parallel, but deviates by 0.34 eV. Therefore, we expect this will cause the broadening of the peak by $\epsilon=0.17 \text{ eV}$. The effect of this broadening is further discussed in Section V.

Figure 2(c) shows the case of comparable Hund's and Jahn-Teller couplings. We see that the structure becomes more complicated as the features overlap, and the band structure becomes less two-dimensional. The low energy shoulder starting from 1 eV originates from the transition between the opposite spin directions. Finally, Fig. 2(e) shows the case of the Jahn-Teller coupling greater than Hund's coupling. In this case the Hund's feature appears strongly for both σ_{xx} and σ_{zz} , whereas the Jahn-Teller feature is now almost completely absent in σ_{zz} . Figures 3(a), 3(c), and 3(e) show the results for a lower value of $J_{\text{H}}S_{\text{c}}$, which show similar features as Figs. 2(a), 2(c), and 2(e).

We have also studied the change of the optical conductivity caused by the change of the ordered orbital state. The orbital ordering angle, θ , defined in Section II, is related to the lattice distortion \bar{v} and \bar{w} by

$$\cos 2\theta = -\frac{\bar{v}}{\sqrt{\bar{v}^2 + \bar{w}^2}} \quad (32)$$

For observed \bar{v} and \bar{w} at $T = 0$, $\theta \approx 54^\circ$. We have varied the ratio between \bar{v} and \bar{w} without changing JT splitting $2\lambda\sqrt{\bar{v}^2 + \bar{w}^2}$. The results are shown in Fig. 4. When $\theta = \pi/6$, the orbital ordering is $x^2 - z^2/y^2 - z^2$ type, and when $\theta = \pi/3$, $3x^2 - r^2/3y^2 - r^2$ type. When $\theta = \pi/4$, orbital state is between the two configurations, and $\bar{v} = 0$, i.e., there is no uniform distortion. As orbital ordering changes from $x^2 - z^2/y^2 - z^2$ to $3x^2 - r^2/3y^2 - r^2$, total spectral weight of σ_{zz} has substantially decreased. If θ is further varied toward $\theta=\pi/2$, which corresponds to non-staggered $x^2 - y^2$ type orbital ordering, then the z -direction conduction becomes smaller. For σ_{xx} , the spectral weight has moved close to the lower edge without appreciable change in the total spectral weight.

B. At T=300 K

The model described above is appropriate to describe the optical conductivity when the spin and lattice degrees of freedom are perfectly ordered at $T=0$ K. If the temperature is non-zero, then the core spins will fluctuate from the ground state configuration. In the actual material, long range order is lost at $T_{\text{N}} \approx 140$ K. Therefore, by room temperature it is reasonable to assume that the core spins are completely disordered. In principle, similar considerations apply to the lattice degrees of freedom, but because room temperature is much lower than the structural transition temperature 800 K, we may neglect lattice fluctuation and assume a static JT distortion.

To describe the system at $T_{\text{N}} \ll T \ll 800$ K, we develop the effective Hamiltonian in the following way. Instead of choosing spin basis along a fixed direction independent of sites, we choose \uparrow on site \vec{i} as the direction of e_g electron parallel to the core spin on site \vec{i} , and \downarrow as its opposite direction. Therefore, the Hund coupling energy is

$$H_{\text{Hund}} = 2J_{\text{H}}S_{\text{c}} \sum_{\vec{i}, a} d_{\vec{i}, a, \downarrow}^\dagger d_{\vec{i}, a, \downarrow}. \quad (33)$$

H_{μ} and H_{JT} do not change their forms by the change of spin basis. We define the angle between the core spin directions on site \vec{i} and on site $\vec{i} + \vec{\delta}$ as $\theta_{\vec{i}, \vec{i} + \vec{\delta}}$, so that the kinetic energy is given by

$$\begin{aligned}
H_{\text{KE}} = & -\frac{1}{2} \sum_{\vec{i}, \vec{\delta}, a, b} t_{\vec{\delta}}^{ab} \left[\cos\left(\frac{\theta_{\vec{i}, \vec{i}+\vec{\delta}}}{2}\right) d_{ia\uparrow}^\dagger d_{i+\vec{\delta}b\uparrow} + \cos\left(\frac{\theta_{\vec{i}, \vec{i}+\vec{\delta}}}{2}\right) d_{ia\downarrow}^\dagger d_{i+\vec{\delta}b\downarrow} \right. \\
& \left. + \sin\left(\frac{\theta_{\vec{i}, \vec{i}+\vec{\delta}}}{2}\right) d_{ia\uparrow}^\dagger d_{i+\vec{\delta}b\downarrow} + \sin\left(\frac{\theta_{\vec{i}, \vec{i}+\vec{\delta}}}{2}\right) d_{ia\downarrow}^\dagger d_{i+\vec{\delta}b\uparrow} + H.c. \right]. \quad (34)
\end{aligned}$$

This new representation of the Hamiltonian reduces to the previous H_{tot} at $T=0$ K. At $T \gg T_N$, $\theta_{\vec{i}, \vec{i}+\vec{\delta}}$ will be completely random. Therefore, we argue it is appropriate to average the Hamiltonian by setting $\langle \cos(\theta_{\vec{i}, \vec{i}+\vec{\delta}}/2) \rangle = \langle \sin(\theta_{\vec{i}, \vec{i}+\vec{\delta}}/2) \rangle = 2/3$, which gives the following effective kinetic energy term

$$\begin{aligned}
H_{\text{KE}}^{\text{eff}} = & -\frac{1}{3} \sum_{\vec{i}, \vec{\delta}, a, b} t_{\vec{\delta}}^{ab} \left[d_{ia\uparrow}^\dagger d_{i+\vec{\delta}b\uparrow} + d_{ia\downarrow}^\dagger d_{i+\vec{\delta}b\downarrow} \right. \\
& \left. + d_{ia\uparrow}^\dagger d_{i+\vec{\delta}b\downarrow} + d_{ia\downarrow}^\dagger d_{i+\vec{\delta}b\uparrow} + H.c. \right]. \quad (35)
\end{aligned}$$

Transforming into \vec{k} space yields the effective total Hamiltonian shown in the Appendix B.

At room temperature, the core spin directions are fluctuating in time and space, which broadens the levels. To incorporate this physics, we introduce a phenomenological broadening Γ , leading to the following expression of the optical conductivity.

$$\begin{aligned}
& \text{Re}[\sigma_{aa}] \\
& = \frac{1}{\omega a_0^3} \frac{1}{(2\pi)^3} \int_S d\vec{k} \int \int dE dE' \sum_{E_j(\vec{k}) < \mu, E_{j'}(\vec{k}) > \mu} \frac{\epsilon |(ea_0/\hbar) 2 \sin k_a B'_a(\vec{k})_{jj'}|^2}{[\hbar\omega - E' + E]^2 + \epsilon^2} \frac{\Gamma/\pi}{[E' - E_{j'}(\vec{k})]^2 + \Gamma^2} \\
& \quad \frac{\Gamma/\pi}{[E - E_j(\vec{k})]^2 + \Gamma^2} \\
& = \frac{1}{\omega a_0^3} \frac{1}{(2\pi)^3} \int_S d\vec{k} \sum_{E_j(\vec{k}) < \mu, E_{j'}(\vec{k}) > \mu} \frac{2\Gamma |(ea_0/\hbar) 2 \sin k_a B'_a(\vec{k})_{jj'}|^2}{[\hbar\omega - E_{j'}(\vec{k}) + E_j(\vec{k})]^2 + (2\Gamma)^2}, \quad (36)
\end{aligned}$$

where

$$B'_a(\vec{k}) = M'(\vec{k})^\dagger T'_a M'(\vec{k}), \quad (37)$$

$$T'_x = \frac{2}{3} \begin{pmatrix} t_x & 0 & t_x & 0 \\ 0 & -t_x & 0 & -t_x \\ t_x & 0 & t_x & 0 \\ 0 & -t_x & 0 & -t_x \end{pmatrix}, \quad (38)$$

$$T'_y = \frac{2}{3} \begin{pmatrix} t_y & 0 & t_y & 0 \\ 0 & -t_y & 0 & -t_y \\ t_y & 0 & t_y & 0 \\ 0 & -t_y & 0 & -t_y \end{pmatrix}, \quad (39)$$

$$T'_z = \frac{2}{3} \begin{pmatrix} t_z & 0 & t_z & 0 \\ 0 & t_z & 0 & t_z \\ t_z & 0 & t_z & 0 \\ 0 & t_z & 0 & t_z \end{pmatrix}, \quad (40)$$

$M'(\vec{k})$ is the matrix diagonalizing H_k^{eff} in the Appendix B, S is defined in the Appendix B, and $t_{x,y,z}$ is the 2×2 matrix defined previously. Γ may be estimated from the root mean square fluctuation in the hopping; we find

$$\Gamma \approx t_o \sqrt{\langle \cos^2(\theta/2) \rangle - \langle \cos(\theta/2) \rangle^2} \approx \frac{t_o}{3\sqrt{2}}. \quad (41)$$

The general features of σ_{xx} and σ_{zz} at $T \gg T_N$ are these: Because we have random spin directions along both x and z directions, both σ_{xx} and σ_{zz} show JT, Hund, and JT+Hund peaks. Due to the anisotropy of the lattice distortion, we still expect anisotropy in the peak intensity. The broadening due to random spin directions means the peaks become smoother than the $T=0$ K case.

Optical conductivities calculated for room temperature are shown in Figs. 2(b), 2(d), and 2(f). For this calculation, we use the same λ , t_o , and $J_H S_c$ as in Figs. 2(a), 2(c), and 2(e), but we use the room temperature lattice parameters, which differ slightly from the 0 K lattice parameters. We obtain $\bar{w}=0.417$ Å and $\bar{v}=0.155$ Å from Ref. 15. As expected, the peaks are substantially broadened and indeed in Figs. 2(d) and 2(f) only two peaks are visible. Figures 3(b), 3(d), and 3(f) show similar results, obtained for the parameters used in Figs. 3(a), 3(c), and 3(e). The upturn of the optical conductivity at around zero frequency is an artifact of the crude consideration of the fluctuation in our model.

We have calculated the variation of spectral weight with temperature and parameter values; the results obtained by Eqs. (21) and (31) are consistent, and shown in the Table I. It shows that at $T=0$ K, K_{xx} sensitively decreases as λ increases, but insensitive to $J_H S_c$, and K_{zz} decreases as λ or $J_H S_c$ increases, which can be understood from the spin and lattice configuration at $T=0$ K. On the other hand, at $T=300$ K, both K_{xx} and K_{zz} have moderate dependence on both λ and $J_H S_c$, which originates from the paramagnetic spin configuration. Temperature dependence of the total spectral weight is relatively weak, even though the spectral weight of each peak depends sensitively on temperature. Particularly, when the Jahn-Teller splitting is the much less than the Hund's splitting (as in Figs. 2(a) and 2(b)), it is possible to identify the lowest energy feature at both 0 K and 300 K as arising from transitions between the parallel-spin but different Jahn-Teller states, and to determine the spectral weight in this feature. When we define

$$K_{a,JT} = \frac{2\hbar^2 a_0}{\pi e^2} \int_{JT\text{peak}} d\omega \sigma_{aa}(\omega), \quad (42)$$

we find $K_{x,JT}^{0K}=0.271$ eV, $K_{x,JT}^{300K}=0.151$ eV for Figs. 2(a) and 2(b), whose ratio is between $1/2$ and $2/3$, as predicted in Ref. 4. The extra $T=0$ K JT spectral weight is pulled down from higher energy peaks as the spin disorder is decreased. It is also noteworthy that the peak shape is more asymmetric at $T = 0$ K than at $T = 300$ K, due to the 2-d character.

We now compare our results to data. This comparison is preliminary because the available data disagree. Optical conductivity for polycrystalline LaMnO_3 was measured at room temperature by Jung *et al.*²¹ Because the crystal directions are random in polycrystalline samples, the observed quantity is $\sigma_{\text{av}} = 2\sigma_{xx}/3 + \sigma_{zz}/3$, which we have also plotted in Fig. 5 (We assume here that the crystallite size is large.). Figure 5(a) shows the results for the parameter values determined from band fitting. The data in Ref. 21 exhibit two

main structures; a lower peak centered at 1.9 eV with maximum intensity $420 \text{ } \Omega^{-1}\text{cm}^{-1}$ and $K_{av,JT} = 2K_{x,JT}/3 + K_{z,JT}/3 \approx 0.115 \text{ eV}$, and a peak centered at around 4.5 eV with a much larger intensity. They attribute the 4.5 eV feature to $e_g - O_{2p}$ transitions beyond the scope of our model, and assign the peak at 1.9 eV to JT-split $e_g - e_g$ transitions within the parallel spin manifold, which we agree with. In this interpretation, the transitions to the reversed spin states are obscured by Mn-O transition. Recently, room temperature optical reflectivity spectra using a cleaved single crystal surface of $\text{La}_{1-x}\text{Sr}_x\text{MnO}_3$ have been measured by Takenaka *et al.*²² Although it is referred to as a single crystal, we believe that the sample of LaMnO_3 is micro-twined. In their results, the Jahn-Teller peak appears at around 2.5 eV, having maximum intensity around $600 \text{ } \Omega^{-1}\text{cm}^{-1}$ with width around 1.5 eV, corresponding to $K_{av,JT} \approx 0.141 \text{ eV}$, and the Mn-O peak appears at 5 eV with maximum intensity $2800 \text{ } \Omega^{-1}\text{cm}^{-1}$. Similar results were obtained by Okimoto *et al.*³ Takenaka *et al.*'s results show a weak shoulder at 1.9 eV, which our model cannot explain.

From Fig. 5(a), one sees that, if the Jahn-Teller interaction were the only important one, the observed lattice distortions would lead to a peak in σ_{av} at 1.2 eV with maximum intensity $\approx 1200 \text{ } \Omega^{-1}\text{cm}^{-1}$, width $\approx 1.0 \text{ eV}$, and $K_{av,JT} = 0.223 \text{ eV}$. The maximum intensity or spectral weight is much larger than observed in either experiment and the peak position is lower. From Fig. 5(c), we see that the data of Ref. 22 may be approximately modeled by use of a stronger electron lattice coupling (or larger amplitude lattice distortion), which moves the peak to higher energy and reduces its spectral weight. The data in Ref. 21 are very difficult to reconcile with theory, because as can be seen from Fig. 3(b), one cannot simultaneously fit the peak amplitude and energy: choosing interaction parameters to fit the peak position leads to an amplitude, which is too large. The combination of peak energy and amplitude could only be explained if the actual hopping were rather smaller than the band theory value (say $t_o \approx 0.4 \text{ eV}$ rather than 0.6 eV).

Further optical data would be very desirable (especially measurements at lower T). For the present we assume the Takenaka *et al.*'s data are correct, and consider their interpretation in more detail. We believe that the combination of band calculation and estimates from the crystallography data adequately fix the magnitude of the Jahn-Teller splitting. We therefore believe that the differences between the Takenaka *et al.* data and Fig. 5(a) are mainly due to the Coulomb interaction whose effects we study in the next section.

IV. COULOMB INTERACTION

We now add an on-site Hubbard-type Coulomb repulsion to our Hamiltonian. Because we have 2 orbital and 2 spin states on each site, we have in principle 6 different Coulomb repulsion terms, which may be generally written (\hat{n} is the density operator)

$$H_{\text{Coulomb}} = \sum_{\vec{i}} \sum_{a \neq b} \sum_{\alpha \neq \beta} U_{(\alpha,\beta),(a,b)} \hat{n}_{\vec{i},\alpha,a} \hat{n}_{\vec{i},\beta,b} \quad (43)$$

For simplicity we study this Hamiltonian in the Hartree-Fock approximation, which we believe is reasonably accurate for the simple quantities (peak position and spectral weight) important for our analysis. Corrections to the Hartree-Fock approximation are due to quantum fluctuations. We have compared Hartree-Fock to exact results for the case of strongest

fluctuations, namely the one-dimensional Hubbard model, and find agreement to within 30% for spectral weight²³ (peak positions are not available). We believe that in the case of present interest, the combination of three dimensionality, the large core spins, and the localization due to the electron-phonon interaction renders the Hartree-Fock approximation sufficiently accurate.

In the approximation, one of the two density operators is replaced by its expectation value, which is determined self-consistently. The approximation explicitly breaks symmetry in spin and orbital space, so the issue of basis choice arises. We choose the orbital basis picked out by the observed lattice distortion and the spin basis picked out by the magnetic ordering. We refer the higher and lower lying orbital states by $+$ and $-$ respectively, and the spin states by \uparrow and \downarrow defined previously. The mean-field Hamiltonian may then be written as

$$H_{\text{Coulomb}}^{\text{MF}} = \sum_{\vec{i}} U_{\uparrow+} d_{i\uparrow+}^{\dagger} d_{i\uparrow+} + U_{\uparrow-} d_{i\uparrow-}^{\dagger} d_{i\uparrow-} + U_{\downarrow+} d_{i\downarrow+}^{\dagger} d_{i\downarrow+} + U_{\downarrow-} d_{i\downarrow-}^{\dagger} d_{i\downarrow-}, \quad (44)$$

where $U_{\uparrow,+} = U_{\uparrow\uparrow+-} < \hat{n}_{\uparrow-} > + U_{\uparrow\downarrow++} < \hat{n}_{\downarrow+} > + U_{\uparrow\downarrow+-} < \hat{n}_{\downarrow-} >$, etc..

Eq. (44) may be reorganized into a term proportional to the total e_g density operator, which renormalizes the chemical potential and is of no interest, a term which couples to the total e_g spin operator and changes the Hund's coupling, and terms which renormalize the local Jahn-Teller splitting in a manner which differs for electrons locally parallel and antiparallel to the core spin. Therefore, $H_{\text{JT}} + H_{\text{Hund}} + H_{\text{Coulomb}}^{\text{MF}}$ can be cast into the following form.

$$H_{\text{JT}} + H_{\text{Hund}} + H_{\text{Coulomb}}^{\text{MF}} = \sum_i \lambda'_{\uparrow} \sqrt{\bar{v}^2 + \bar{w}^2} (\hat{n}_{i\uparrow+} - \hat{n}_{i\uparrow-}) + \lambda'_{\downarrow} \sqrt{\bar{v}^2 + \bar{w}^2} (\hat{n}_{i\downarrow+} - \hat{n}_{i\downarrow-}) \\ + 2J'_{\text{H}} S_{\text{c}} (\hat{n}_{i\downarrow+} + \hat{n}_{i\downarrow-}), \quad (45)$$

where

$$\lambda'_{\uparrow} = \lambda + \frac{U_{\uparrow+} - U_{\uparrow-}}{2\sqrt{\bar{v}^2 + \bar{w}^2}}, \quad (46)$$

$$\lambda'_{\downarrow} = \lambda + \frac{U_{\downarrow+} - U_{\downarrow-}}{2\sqrt{\bar{v}^2 + \bar{w}^2}}, \quad (47)$$

$$2J'_{\text{H}} S_{\text{c}} = 2J_{\text{H}} S_{\text{c}} + \frac{1}{2}(U_{\downarrow+} + U_{\downarrow-} - U_{\uparrow+} - U_{\uparrow-}). \quad (48)$$

Because the hopping matrices are defined in $|\psi_1\rangle$ and $|\psi_2\rangle$ orbital basis, we need to transform the basis. For this purpose, it turns out useful to define

$$\lambda'_{\uparrow} = \lambda'_{av} + \delta\lambda', \quad (49)$$

$$\lambda'_{\downarrow} = \lambda'_{av} - \delta\lambda'. \quad (50)$$

If we transform into k space in $|\psi_1\rangle$ and $|\psi_2\rangle$ basis, we obtain the Hamiltonian to calculate optical conductivity. Details are shown in the Appendix C along with the expression of the number operators.

As the simplest case, we consider the case where $U_{(\alpha,\beta),(a,b)} = U$, independent of (α, β) and (a, b) . For this case, we use t_o , λ , and $J_{\text{H}} S_{\text{c}}$ obtained previously and determine the values

of U by calculating optical conductivity at $T=300$ K and comparing with experimental JT peak position. For the JT peak at 2.5 eV in Takenaka *et al.*'s results, we obtain $U=1.6$ eV. The obtained value of U is close to the difference of the experimental peak position and the calculated peak position for the $U=0$ case. The room temperature results are shown in Figs. 6(b) and 6(d). As we increase the value of U , the peak position shifts upwards by $\approx U$, and the peak intensity decreases. For $U=1.6$ eV, the calculated maximum peak intensity is $730 \Omega^{-1}\text{cm}^{-1}$, width 1.2 eV, and $K_{\text{av,JT}}^{300\text{K}} \approx 0.145$ eV. Therefore, the calculated spectral weight is close to the observed spectral weight. With these determined values of U , we calculate $T=0$ K results shown in Figs. 6(a) and 6(c), from which we can see the anisotropy and temperature dependence of optical conductivity.

In the no-hopping case, the energy levels on each site are $-\lambda'_{\uparrow}\sqrt{\bar{v}^2 + \bar{w}^2}$, $\lambda'_{\uparrow}\sqrt{\bar{v}^2 + \bar{w}^2}$, $2J'_{\text{H}}S_{\text{c}} - \lambda'_{\downarrow}\sqrt{\bar{v}^2 + \bar{w}^2}$, and $2J'_{\text{H}}S_{\text{c}} + \lambda'_{\downarrow}\sqrt{\bar{v}^2 + \bar{w}^2}$. Even though the finite hopping gives dispersion to the energy levels, the peak positions are close to the energy differences between different levels. Therefore, the JT peak position is close to $2\lambda'_{\uparrow}\sqrt{\bar{v}^2 + \bar{w}^2}$, the Hund peak position is close to $2J'_{\text{H}}S_{\text{c}} + (\lambda'_{\uparrow} - \lambda'_{\downarrow})\sqrt{\bar{v}^2 + \bar{w}^2}$, and the JT+Hund peak position is close to $2J'_{\text{H}}S_{\text{c}} + (\lambda'_{\uparrow} + \lambda'_{\downarrow})\sqrt{\bar{v}^2 + \bar{w}^2}$. To see the effect of different type of Coulomb interaction and other parameters, we use different values of λ'_{\downarrow} , $J'_{\text{H}}S_{\text{c}}$ and calculate optical conductivities without changing the value of λ'_{\uparrow} . We observe that the JT peak position and spectral weight do not change very much. Therefore even if we use a more general Coulomb interaction, with $U_{(\alpha,\beta),(a,b)}$ dependent on the indices, as far as we fix the JT peak position by fixing λ'_{\uparrow} , its spectral weight does not change very much.

For the above model, we also calculate the variation of the level occupancies as a function of U . The results for the lowest lying orbital $< \hat{n}_{\uparrow,-} >$ are shown in Fig. 7 for $T=0$ K and $T=300$ K, which shows that as U increases, the e_g electrons are more likely to have spins parallel to the core spins and stay in the ground state of the local lattice distortion. The curves however show that the value of U required to fit Takenaka *et al.*'s data does not change the ground state occupancy much.

V. COMPARISON WITH LSDA CALCULATION OF OPTICAL CONDUCTIVITY

Terakura *et al.* have calculated the $T=0$ K optical conductivity using optical matrix elements and energies obtained from their LSDA band calculation.⁹ Their conductivity is strikingly different from ours in two respects. First, the form is different: the sharp peaks we find are absent in their calculation. We suspect that the difference is due in large part to the $0.01 \text{ Ry} \approx 0.14 \text{ eV}$ level broadening employed in Ref. 9. Figure 8 shows the effect of introducing an artificial broadening, ϵ , into our calculation; the result is to be compared with Fig. 2(a). This figure shows that as broadening is increased, the peaks diminish in amplitude and become more symmetrical (although there is always more asymmetry in our calculation than in Ref. 9). Particularly, the Hund peak in σ_{zz} is expected to have additional broadening of about 0.17 eV as mentioned in Section III. Therefore, if we include 0.01 Ry broadening assumed in Ref. 9, the total broadening for the Hund peak in σ_{zz} will be $\epsilon \approx 0.3 \text{ eV}$, which explains the absence of this peak feature in Ref. 9. Therefore, we believe the level

broadening along with the presence, in the calculation of Ref. 9, of other bands, accounts for the difference in line shape.

A far more serious discrepancy is the difference in spectral weights. The area under the lowest conductivity peak in Ref. 9 is about a factor of 4 smaller than in our calculation. This difference seems not to be caused by a trivial error: in our calculation, the kinetic energies obtained from Eq. (21), from Eq. (31) (i.e., direct integration of σ), or from the Hellman-Feynman theorem agree. According to Hellman-Feynman theorem, $K = K_{xx} + K_{yy} + K_{zz}$ can be found from the ground state energy E_0/N_{Mn} by

$$K = -t_0 \frac{d(E_0/N_{Mn})}{dt_0}, \quad (51)$$

where t_0 is the hopping parameter defined in Section II. At $T=0$ K, we have calculated E_0 as the sum of energies of the filled bands,

$$\frac{E_0}{N_{Mn}} = \frac{2}{(2\pi)^3} \int_R d\vec{k} [E_1(\vec{k}) + E_2(\vec{k})] \quad (52)$$

and evaluated K using Eq. (51). The result obtained in this way is consistent with the results in Table I.

We examine the size of the possible error due to the following two approximations we have made: First, we have assumed that the hopping between Mn ions, which originates from Mn-O hopping, can be effectively represented without explicit consideration of O band. Second, we have used tight binding approximation.

To study the effects of Mn-O hybridization on the conductivity in the dominantly Mn bands, we consider a simple model of a 1-d Mn-O chain along x direction. Each unit cell contains one Mn ion at position $R_i^{\text{Mn}} = n_i a_0$ with a d-orbital represented by d_i^\dagger , and one oxygen ion at position $R_i^{\text{O}} = (n_i + 1/2)a_0$ with a p-orbital represented by p_i^\dagger . We consider a Mn-O hopping of magnitude $t_{\text{Mn-O}}$ and choose sign to reflect the symmetry of the O p-orbital (the sign can be removed by change of k space origin). In addition, to model the Jahn-Teller distortion, we consider alternating periodic potential Δ on the Mn site. We represent the energy of the d-level relative to the p-level by V . For simplicity we assume spinless electrons. This can be represented by the following Hamiltonian.

$$H = -\frac{t_{\text{Mn-O}}}{2} \sum_i (d_i^\dagger p_i - p_i^\dagger d_{i+1} - d_{i+1}^\dagger p_i + p_i^\dagger d_i + H.c.) \\ + \sum_i \frac{\Delta}{2} (-1)^i d_i^\dagger d_i - V p_i^\dagger p_i. \quad (53)$$

We obtain the exact band structure and optical conductivity and compare this to the band structure and conductivity obtained from nearest-neighbor tight-binding fit to the two uppermost (Mn-dominant) bands. The difference turns out small. The effective tight binding Hamiltonian is

$$H_{\text{eff}} = -\frac{t_{\text{eff}}}{2} \sum_i (d_i^\dagger d_{i+1} + d_i^\dagger d_{i-1} + H.c.) + \sum_i \frac{\Delta_{\text{eff}}}{2} (-1)^i d_i^\dagger d_i \quad (54)$$

By transforming into k space, we can find band structure for H and H_{eff} . The band structure of H_{eff} is simply given by

$$E = \pm \sqrt{4t_{\text{eff}}^2 \cos^2 k + \frac{\Delta_{\text{eff}}^2}{4}} \quad (55)$$

For given $t_{\text{Mn-O}}$, Δ , and V , we can fit the band structure of H_{eff} to that of H to determine t_{eff} and Δ_{eff} .

For $t_{\text{Mn-O}}=2.0$ eV, $\Delta=1.0$ eV, we try $V = 1.0$ eV and 10 eV. The obtained d-bands are shown in Figs. 9(a) and 9(b) ($V=1.0$ eV and 10 eV, respectively) as solid lines, along with the best tight binding fit as dotted lines. Fitted parameter values are $t_{\text{eff}}=0.88$ eV, $\Delta_{\text{eff}}=0.59$ eV for $V=1.0$ eV, and $t_{\text{eff}}=0.35$ eV, $\Delta_{\text{eff}}=0.93$ eV for $V=10$ eV. It shows that when $V=1.0$ eV, the fitting has error of 10 % of d-band width (comparable to the error in the fits used in Section II - IV), but when $V=10$ eV, the fitting has negligible error. For these two cases, we assume half filling, and calculate optical conductivities shown in Figs. 9(c) and 9(d). The insets show the integrated spectral weight, $K(\hbar\omega) = (2\hbar^2 a_0 / \pi e^2) \int_0^{\hbar\omega} \sigma(\omega) d\omega$. In this calculation, we assumed the Mn-Mn distance is $a_0=4.034$ Å, and the cross sectional area perpendicular to the direction of the chain is a_0^2 . For $V=10$ eV, the two calculations give almost identical results. For $V=1.0$ eV, the tight binding fit has about 25 % larger spectral weight. We therefore expect our Mn-only approximation yields errors ≈ 25 %.

Next, to estimate the error of the tight binding approximation (i.e., of the Peierls approximation to the optical matrix elements), we consider the following Kronig-Penney model.

$$\hat{H} = -\frac{1}{2} \frac{d^2}{dx^2} + \sum_{n=-\infty}^{\infty} \left[\frac{\lambda_1}{2} \delta(x - 2n - 1) + \frac{\lambda_2}{2} \delta(x - 2n) \right] \quad (56)$$

where $\lambda_1, \lambda_2 < 0$, $\hbar=m_e=e=1$, and spinless electrons are assumed for simplicity. Once the values of λ_1 and λ_2 are given, we can find the band structure, the eigenstates $\psi_k(x)$, and the optical conductivity, and compare this to the Peierls approximation. The band structure has two bands; at $n=1/2$, one is filled and the other is empty. Therefore, we can calculate the optical conductivity via

$$\sigma = \frac{1}{\omega} \frac{1}{2\pi} \int_{-\frac{\pi}{2}}^{\frac{\pi}{2}} \frac{\left| \langle 2, k | \frac{d}{dx} | 1, k \rangle \right|^2 \epsilon}{[\omega - E_2(k) + E_1(k)]^2 + \epsilon^2} d\omega, \quad (57)$$

where 1 and 2 are the band indices. For $\lambda_1 = -4$, $\lambda_2 = -5$, we calculate the exact band structure, shown in Fig. 10(a) along with the best tight binding fit from Eq. (54) ($t_{\text{eff}}=1.33$, $\Delta_{\text{eff}}=0.6$). It shows that the error is about 7 % of the total band width. Figure 10(b) shows the calculated optical conductivity for the exact K-P model and tight binding fit. The spectral weight of the tight binding fit is about 20 % larger than that of exact result, as shown in the inset.

In our calculation of optical conductivity, our band fitting has error about 0.2 eV, which corresponds to about 5 % of total Mn $e_g \uparrow$ band width. So, we expect our approximation has similar size error in spectral weight as the two cases considered above. Therefore, we expect that our calculated optical conductivity may have overestimated spectral weight by

about 20 %, but not 400 %. Therefore, we believe that within this error, our approximations are valid.

The relation between the kinetic energy and the optical spectral weight follows from the two assumptions of gauge invariance and reasonably localized d-electron wave functions. The success of the tight binding fit confirms this localized character. A tight binding parameterization of the band structure has been used to study $\sigma(\omega)$ in other correlated electron contexts,^{19,24} and works well in high T_c case. The apparent discrepancy found here for the manganite, is an important issue for future research.

VI. CONCLUSION

We have calculated the optical conductivity of LaMnO_3 and have shown that the available data are consistent with the band theory estimation for hopping parameter and e_g level splitting. Our main prediction for the change in functional form and magnitude of σ as T is decreased below T_N is contained in Fig. 6. Experimental determination of the Hund's coupling as well as final validation of the model must await definitive measurements of the magnitude and temperature dependence of $\sigma(\omega)$.

In conclusion, we comment on the implications of our results. First, we note that the estimate of the electron-lattice coupling derived from band theory is in good agreement with that derived directly from crystallography data. Second, we observe that the electron-lattice interaction by itself does not account for the magnitude of the gap or the spectral weight in the absorption spectrum. A Coulomb interaction $U \approx 1.6$ eV is also required. This value puts LaMnO_3 in the weak-intermediate coupling range: the Coulomb interaction is approximately 40% of the full band width $6 t_o \approx 3.6$ eV. In the simple one-band Hubbard model, a Coulomb interaction of this size (relative to the band width) does not significantly affect properties (such as optical spectral weights) at reasonable dopings of order 0.2 or larger. The effects of this moderate Coulomb coupling on properties of models of doped manganites deserve further attention. Many authors have argued on the basis of photoemission data²⁵ that the Coulomb repulsion is large (5-10 eV); however as noted by the experimentalists themselves, because the manganites are charge-transfer rather than Mott-Hubbard materials (as are the high- T_c superconductors) the U measured in photoemission is not directly relevant to the low ($\hbar\omega < 4$ eV) energy physics of interest here.

Our data analysis focuses on robust features (peak positions and spectral weights) and is insensitive to the approximations we made. Uncertainties in the tight binding parameterization of the band structure leads to an error ≈ 0.2 eV in peak position, which is not important here; the consistency of the peak position and spectral weights leads us to believe the band theory estimates of t_o are reasonably accurate. Uncertainties in the estimates of electron-phonon coupling λ could change our estimated Coulomb repulsion by around 0.2 eV. We note however that we have not included any excitonic effects arising from the first neighbor interactions such as those proposed by Maekawa *et al.*²⁶ At $T=0$ K, the two-dimensional character and general flatness of the bands suggest that these might be important and interesting to look for.

The crucial prediction of the present model is the dramatic change in optical absorption with temperature. This change is a robust feature of the model, and comes from a dramatic

shift in spectral weight caused by ferromagnetic spin ordering, along with a very nearly two dimensional character of the bands at $T \rightarrow 0$, caused by the between-planes antiferromagnetism. Early data³ reported only a weak temperature dependence of the optical absorption; if these data are reproduced, then our fundamental picture of the manganites based on e_g electron with electron-lattice and electron-electron interactions must be modified.

Finally, we note that a troubling discrepancy with band theory calculations exists. Further work is needed to find origin of the differences.

We thank H. Drew, S. Louie, O. Myrasov, and M. Quijada for helpful discussions, and NSF-DMR-9705182 and the University of Maryland MRSEC for support.

APPENDIX A:

Without considering the Coulomb repulsion, the total Hamiltonian at $T=0$ K is given by the following expression.

$$H_{\text{tot}} = \sum_{\alpha=\uparrow,\downarrow, \vec{k} \in R} d_{\alpha, \vec{k}}^\dagger H_{\alpha, \vec{k}} d_{\alpha, \vec{k}}, \quad (\text{A1})$$

where

$$d_{\alpha, \vec{k}}^\dagger = (d_{1, \vec{k}, \alpha}^\dagger, d_{2, \vec{k}, \alpha}^\dagger, d_{1, \vec{k}+(\pi, \pi, 0), \alpha}^\dagger, d_{2, \vec{k}+(\pi, \pi, 0), \alpha}^\dagger, d_{1, \vec{k}+(0, 0, \pi), \alpha}^\dagger, d_{2, \vec{k}+(0, 0, \pi), \alpha}^\dagger, d_{1, \vec{k}+(\pi, \pi, \pi), \alpha}^\dagger, d_{2, \vec{k}+(\pi, \pi, \pi), \alpha}^\dagger), \quad (\text{A2})$$

$$H_{\vec{k}, \alpha} = \begin{pmatrix} M_1 + G + V & W & G_\alpha & 0 \\ W & M_2 + G + V & 0 & G_\alpha \\ G_\alpha & 0 & M_3 + G + V & W \\ 0 & G_\alpha & W & M_4 + G + V \end{pmatrix}, \quad (\text{A3})$$

$$M_1 = \begin{pmatrix} -\frac{t_0}{2}(\cos k_x + \cos k_y + 4 \cos k_z) & \frac{\sqrt{3}t_0}{2}(\cos k_x - \cos k_y) \\ \frac{\sqrt{3}t_0}{2}(\cos k_x - \cos k_y) & -\frac{3t_0}{2}(\cos k_x + \cos k_y) \end{pmatrix}, \quad (\text{A4})$$

$$M_2 = \begin{pmatrix} \frac{t_0}{2}(\cos k_x + \cos k_y - 4 \cos k_z) & -\frac{\sqrt{3}t_0}{2}(\cos k_x - \cos k_y) \\ -\frac{\sqrt{3}t_0}{2}(\cos k_x - \cos k_y) & \frac{3t_0}{2}(\cos k_x + \cos k_y) \end{pmatrix}, \quad (\text{A5})$$

$$M_3 = \begin{pmatrix} -\frac{t_0}{2}(\cos k_x + \cos k_y - 4 \cos k_z) & \frac{\sqrt{3}t_0}{2}(\cos k_x - \cos k_y) \\ \frac{\sqrt{3}t_0}{2}(\cos k_x - \cos k_y) & -\frac{3t_0}{2}(\cos k_x + \cos k_y) \end{pmatrix}, \quad (\text{A6})$$

$$M_4 = \begin{pmatrix} \frac{t_0}{2}(\cos k_x + \cos k_y + 4 \cos k_z) & -\frac{\sqrt{3}t_0}{2}(\cos k_x - \cos k_y) \\ -\frac{\sqrt{3}t_0}{2}(\cos k_x - \cos k_y) & \frac{3t_0}{2}(\cos k_x + \cos k_y) \end{pmatrix}, \quad (\text{A7})$$

$$G = \begin{pmatrix} J_H S_c & 0 \\ 0 & J_H S_c \end{pmatrix}, \quad (\text{A8})$$

$$G_\uparrow = -G, \quad (\text{A9})$$

$$G_\downarrow = G, \quad (\text{A10})$$

$$V = \begin{pmatrix} \lambda \bar{v} & 0 \\ 0 & -\lambda \bar{v} \end{pmatrix}, \quad (\text{A11})$$

$$W = \begin{pmatrix} 0 & -\lambda\bar{w} \\ -\lambda\bar{w} & 0 \end{pmatrix}, \quad (\text{A12})$$

$$R = \{\vec{k} ||k_x| + |k_y| < \pi \text{ and } |k_z| < \pi/2\}. \quad (\text{A13})$$

APPENDIX B:

Without considering the Coulomb repulsion, the effective total Hamiltonian at $T=300$ K is given by the following expression.

$$H_{\text{tot}}^{\text{eff},300\text{K}} = \sum_{\vec{k} \in S} d_{\vec{k}}^\dagger H_{\vec{k}}^{\text{eff},300\text{K}} d_{\vec{k}}, \quad (\text{B1})$$

where

$$d_{\vec{k}}^\dagger = (d_{1,\vec{k},\uparrow}^\dagger, d_{2,\vec{k},\uparrow}^\dagger, d_{1,\vec{k}+(\pi,\pi,0),\uparrow}^\dagger, d_{2,\vec{k}+(\pi,\pi,0),\uparrow}^\dagger, \\ d_{1,\vec{k},\downarrow}^\dagger, d_{2,\vec{k},\downarrow}^\dagger, d_{1,\vec{k}+(\pi,\pi,0),\downarrow}^\dagger, d_{2,\vec{k}+(\pi,\pi,0),\downarrow}^\dagger), \quad (\text{B2})$$

$$H_{\vec{k}}^{\text{eff},300\text{K}} = \begin{pmatrix} \frac{2}{3}M_1 + V & W & \frac{2}{3}M_1 & 0 \\ W & \frac{2}{3}M_2 + V & 0 & \frac{2}{3}M_2 \\ \frac{2}{3}M_1 & 0 & \frac{2}{3}M_1 + V + 2G & W \\ 0 & \frac{2}{3}M_2 & W & \frac{2}{3}M_2 + V + 2G \end{pmatrix}, \quad (\text{B3})$$

$$S = \{\vec{k} ||k_x| + |k_y| < \pi \text{ and } |k_z| < \pi\}. \quad (\text{B4})$$

M_1 , M_2 , V , W and G are defined in Appendix A.

APPENDIX C:

At $T=0$ K, the total mean field Hamiltonian with the Coulomb interaction,

$$H_{\text{tot}}^{\text{MF}} = \sum_{\alpha=\uparrow,\downarrow, \vec{k} \in R} d_{\alpha,\vec{k}}^\dagger H_{\alpha,\vec{k}}^{\text{MF}} d_{\alpha,\vec{k}}, \quad (\text{C1})$$

has the same form as H_{tot} in the Appendix A with $J_{\text{H}}S_c \rightarrow J'_{\text{H}}S_c$, $\lambda \rightarrow \lambda'_{av}$ and the following additional term.

$$H_{\text{add},T=0\text{K}}^{\text{MF}} = \sum_{\alpha=\uparrow,\downarrow, \vec{k} \in R} d_{\alpha,\vec{k}}^\dagger H_{\text{add},\alpha,\vec{k}}^{\text{MF}} d_{\alpha,\vec{k}}, \quad (\text{C2})$$

where

$$H_{\text{add},\alpha,\vec{k}}^{\text{MF}} = \begin{pmatrix} 0 & 0 & \delta\bar{V}_\alpha & \delta\bar{W}_\alpha \\ 0 & 0 & \delta\bar{W}_\alpha & \delta\bar{V}_\alpha \\ \delta\bar{V}_\alpha & \delta\bar{W}_\alpha & 0 & 0 \\ \delta\bar{W}_\alpha & \delta\bar{V}_\alpha & 0 & 0 \end{pmatrix}, \quad (\text{C3})$$

$$\delta\bar{V}_\alpha = \begin{pmatrix} \delta\lambda'_\alpha \bar{v} & 0 \\ 0 & -\delta\lambda'_\alpha \bar{v} \end{pmatrix}, \quad (C4)$$

$$\delta\bar{W}_\alpha = \begin{pmatrix} 0 & -\delta\lambda'_\alpha \bar{w} \\ -\delta\lambda'_\alpha \bar{w} & 0 \end{pmatrix}, \quad (C5)$$

$$\delta\lambda'_\uparrow = \delta\lambda', \quad (C6)$$

$$\delta\lambda'_\downarrow = -\delta\lambda'. \quad (C7)$$

Similarly, for $T=300$ K the effective mean field total Hamiltonian with the Coulomb interaction,

$$H_{\text{tot}}^{\text{MF},300\text{K}} = \sum_{\vec{k} \in S} d_{\vec{k}}^\dagger H_{\vec{k}}^{\text{MF},300\text{K}} d_{\vec{k}}, \quad (C8)$$

has the same form as $H_{\text{tot}}^{\text{eff},300\text{K}}$ in the Appendix B with $J_{\text{H}}S_{\text{c}} \rightarrow J'_{\text{H}}S_{\text{c}}$, $\lambda \rightarrow \lambda'_{av}$, and the following additional term.

$$H_{\text{add}}^{\text{MF},300\text{K}} = \sum_{\vec{k} \in S} d_{\vec{k}}^\dagger H_{\text{add},\vec{k}}^{\text{MF},300\text{K}} d_{\vec{k}}, \quad (C9)$$

where

$$H_{\text{add},\vec{k}}^{\text{MF},300\text{K}} = \begin{pmatrix} \delta\bar{V} & \delta\bar{W} & 0 & 0 \\ \delta\bar{W} & \delta\bar{V} & 0 & 0 \\ 0 & 0 & -\delta\bar{V} & -\delta\bar{W} \\ 0 & 0 & -\delta\bar{W} & -\delta\bar{V} \end{pmatrix}. \quad (C10)$$

$$\delta\bar{V} = \begin{pmatrix} \delta\lambda'_\uparrow \bar{v} & 0 \\ 0 & -\delta\lambda'_\uparrow \bar{v} \end{pmatrix}, \quad (C11)$$

$$\delta\bar{W} = \begin{pmatrix} 0 & -\delta\lambda'_\uparrow \bar{w} \\ -\delta\lambda'_\uparrow \bar{w} & 0 \end{pmatrix}. \quad (C12)$$

With these Hamiltonians for given $U_{(\alpha,\beta),(a,b)}$, we can repeatedly calculate $\langle \hat{n}_{\beta,b} \rangle$ until its value converges. At $T=0$ K, $\langle \hat{n}_{\alpha,a} \rangle$ is given by the following expression.

$$\langle \hat{n}_{\alpha,a} \rangle = \frac{1}{(2\pi)^3} \int_R d\vec{k} \sum_{j=1,2} [P_\uparrow(\vec{k})^\dagger Q_{\uparrow\alpha a} P_\uparrow(\vec{k})]_{jj} + [P_\downarrow(\vec{k})^\dagger Q_{\downarrow\alpha a} P_\downarrow(\vec{k})]_{jj}, \quad (C13)$$

where

$$Q_{\uparrow\uparrow,\pm} = Q_{\downarrow\downarrow,\pm} = Q_{1\pm}, \quad (C14)$$

$$Q_{\downarrow\uparrow,\pm} = Q_{\uparrow\downarrow,\pm} = Q_{2\pm}, \quad (C15)$$

$$Q_{1\pm} = \begin{pmatrix} A_\pm & B_\pm & A_\pm & B_\pm \\ B_\pm & A_\pm & B_\pm & A_\pm \\ A_\pm & B_\pm & A_\pm & B_\pm \\ B_\pm & A_\pm & B_\pm & A_\pm \end{pmatrix}, \quad (C16)$$

$$Q_{2\pm} = \begin{pmatrix} A_{\pm} & B_{\pm} & -A_{\pm} & -B_{\pm} \\ B_{\pm} & A_{\pm} & -B_{\pm} & -A_{\pm} \\ -A_{\pm} & -B_{\pm} & A_{\pm} & B_{\pm} \\ -B_{\pm} & -A_{\pm} & B_{\pm} & A_{\pm} \end{pmatrix}, \quad (\text{C17})$$

$$A_{\pm} = \begin{pmatrix} \alpha_{\pm}^2/2 & 0 \\ 0 & \beta_{\pm}^2/2 \end{pmatrix}, \quad (\text{C18})$$

$$B_{\pm} = \begin{pmatrix} 0 & \alpha_{\pm}\beta_{\pm}/2 \\ \alpha_{\pm}\beta_{\pm}/2 & 0 \end{pmatrix}, \quad (\text{C19})$$

$$\alpha_{\pm} = \frac{\bar{w}}{\sqrt{2(\bar{v}^2 + \bar{w}^2) \mp 2\bar{v}\sqrt{\bar{v}^2 + \bar{w}^2}}}, \quad (\text{C20})$$

$$\beta_{\pm} = \frac{\bar{v} \mp \sqrt{\bar{v}^2 + \bar{w}^2}}{\sqrt{2(\bar{v}^2 + \bar{w}^2) \mp 2\bar{v}\sqrt{\bar{v}^2 + \bar{w}^2}}}, \quad (\text{C21})$$

and $P_{\alpha}(\vec{k})$ is the matrix diagonalizing $H_{\alpha,\vec{k}}^{\text{MF}}$.

At $T=300$ K,

$$\langle \hat{n}_{\alpha,a} \rangle = \frac{1}{(2\pi)^3} \int_S d\vec{k} \sum_{j=1,2} [P'(\vec{k})^{\dagger} Q'_{\alpha a} P'(\vec{k})]_{jj}, \quad (\text{C22})$$

where

$$Q'_{\uparrow\pm} = \begin{pmatrix} A_{\pm} & B_{\pm} & 0 & 0 \\ B_{\pm} & A_{\pm} & 0 & 0 \\ 0 & 0 & 0 & 0 \\ 0 & 0 & 0 & 0 \end{pmatrix}, \quad (\text{C23})$$

$$Q'_{\downarrow\pm} = \begin{pmatrix} 0 & 0 & 0 & 0 \\ 0 & 0 & 0 & 0 \\ 0 & 0 & A_{\pm} & B_{\pm} \\ 0 & 0 & B_{\pm} & A_{\pm} \end{pmatrix}, \quad (\text{C24})$$

and $P'(\vec{k})$ is the matrix diagonalizing $H_{\vec{k}}^{\text{MF},300\text{K}}$.

REFERENCES

- * On leave from Department of Physics and Astronomy, The Johns Hopkins University, Baltimore, Maryland 21218.
- ¹ see, e.g. the articles in Philos. Trans. R. Soc. London, Ser. A, **356**, No. 1752, pp. 1469-1712 (1998).
- ² E. O. Wollan and W. C. Koehler, Phys. Rev. **100**, 545 (1995).
- ³ Y. Okimoto, T. Katsufuji, T. Ishikawa, T. Arima and Y. Tokura, Phys. Rev. B **55**, 4206 (1997).
- ⁴ M. Quijada, J. Černe, J. R. Simpson, H. D. Drew, K. H. Ahn, A. J. Millis, R. Shreekala, R. Ramesh, M. Rajeswari, and T. Venkatesan, Phys. Rev. B **58**, 16093 (1998).
- ⁵ T. Saitoh, A. E. Bocquet, T. Mizokawa, H. Namatame, A. Fujimori, M. Abbate, Y. Takeda, and M. Takano, Phys. Rev. B **51**, 13942 (1995).
- ⁶ J. Zaanen, G. A. Sawatzky, and J. W. Allen, Phys. Rev. Lett. **55**, 418 (1985).
- ⁷ M. S. Hybertsen and M. Schlüter, Phys. Rev. B **39**, 9028 (1989).
- ⁸ I. Solovyev, N. Hamada, and K. Terakura, Phys. Rev. B **53**, 7158 (1996).
- ⁹ K. Terakura, I. V. Solovyev, and H. Sawada, in *Colossal Magnetoresistive Oxides*, edited by Y. Tokura (Gordon and Breach, Tokyo, 1999).
- ¹⁰ S. Satpathy, Z. S. Popovic, and F. R. Vukajlovic, Phys. Rev. Lett. **76**, 960 (1996).
- ¹¹ S. Satpathy, Z. S. Popovic, and F. R. Vukajlovic, J. Appl. Phys. **79**, 4555 (1996).
- ¹² W. E. Pickett and D. J. Singh, Phys. Rev. B. **53**, 1146 (1996).
- ¹³ P. W. Anderson, *The theory of superconductivity in the high-T_c cuprates* (Princeton University Press, Princeton, NJ, 1997).
- ¹⁴ O. Myrasov, S. Ilani, and A. Freeman (to be published).
- ¹⁵ J. B. A. A. Ellemans, B. van Laar, K. R. van der Veen, and B. O. Loopstra, J. Solid State Chem. **3**, 238 (1971).
- ¹⁶ A. J. Millis, Phys. Rev. B **53**, 8434 (1996).
- ¹⁷ J. H. Jung, T. W. Noh (private communication).
- ¹⁸ A. J. Millis and S. Coppersmith, Phys. Rev. B. **42**, 10807 (1990).
- ¹⁹ E. Dagotto, Rev. Mod. Phys. **66** 763 (1994).
- ²⁰ W. Kohn, Phys. Rev. **113**, A171 (1964).
- ²¹ J. H. Jung, K. H. Kim, D. J. Eom, T. W. Noh, E. J. Choi, J. Yu, Y. S. Kwon, and Y. Chung, Phys. Rev. B **55**, 15489 (1997).
- ²² K. Takenaka, K. Iida, Y. Sawaki, S. Sugai, Y. Moritomo, and A. Nakamura (unpublished).
- ²³ C. A. Stafford, Ph. D. Thesis, Princeton University, 1992.
- ²⁴ D. Baeriswyl, J. Carmelo, and A. Luther, Phys. Rev. B. **33**, 7247 (1986).
- ²⁵ T. Saitoh, A. Sekiyama, K. Kobayashi, T. Mizokawa, A. Fujimori, D. D. Sarma Y. Takeda and M. Takano, Phys. Rev. **B56** 8836 (1997).
- ²⁶ S. Maekawa, J. Magn. Magn. Mater. **177**, 850(1998) and W. Koshibae, Y. Kawamura, I-L Inoue, and S. Maekawa, J. Phys. Soc. Jpn. **66**, 2985(1997).

FIGURES

FIG. 1. Fitted e_g band structure of LaMnO_3 : $t_0 = 0.622$ eV, $2J_{\text{H}}S_{\text{c}} = 2.47$ eV, $\lambda=1.38$ eV/Å, and $\mu=0.4$ eV. $(\pi,0,0)$, $(0,0,0)$, $(\pi/2,\pi/2,\pi/2)$, and $(\pi,0,\pi/2)$ points correspond to M, Γ , R, and A points in Ref. 11 respectively.

FIG. 2. Optical conductivities σ_{xx} (solid lines) and σ_{zz} (dotted lines) for $t_0 = 0.622$ eV, and $2J_{\text{H}}S_{\text{c}} = 2.47$ eV without Coulomb repulsion($U=0$).

FIG. 3. Optical conductivities σ_{xx} (solid lines) and σ_{zz} (dotted lines) for $t_0 = 0.622$ eV, and $2J_{\text{H}}S_{\text{c}} = 2.10$ eV without Coulomb repulsion($U=0$).

FIG. 4. Optical conductivities σ_{xx} (solid lines) and σ_{zz} (dotted lines) for $t_0 = 0.622$ eV, and $2J_{\text{H}}S_{\text{c}} = 2.47$ eV, $\lambda = 1.38$ eV/Å, $U=0$ with different orbital ordering angle θ .

FIG. 5. Average optical conductivities σ_{av} for $t_0 = 0.622$ eV and $2J_{\text{H}}S_{\text{c}} = 2.47$ eV at $T=300$ K without Coulomb repulsion($U=0$).

FIG. 6. Optical conductivities for $t_0 = 0.622$ eV, $2J_{\text{H}}S_{\text{c}} = 2.47$ eV, $\lambda=1.38$ eV/Å, and $U=1.59$ eV.

FIG. 7. Occupancies of the lowest-lying orbital versus U for $t_0 = 0.622$ eV, $2J_{\text{H}}S_{\text{c}} = 2.47$ eV, and $\lambda=1.38$ eV/Å at $T=0$ K and 300 K.

FIG. 8. Optical conductivities σ_{xx} (solid lines) and σ_{zz} (dotted lines) for $t_0 = 0.622$ eV, and $2J_{\text{H}}S_{\text{c}} = 2.47$ eV, $\lambda = 1.38$ eV/Å, $U=0$ with different broadening ϵ .

FIG. 9. Mn d band structures[(a),(b)] and optical conductivities[(c),(d)] of Mn-O chain in a model explicitly considering O p-level (solid lines) and in the best-fit effective Mn-Mn chain model (dotted lines) for $t_{\text{Mn-O}}=2.0$ eV, $\Delta=1.0$ eV, and $V = 1.0$ eV, $t_{\text{eff}}=0.88$ eV, $\Delta_{\text{eff}}= 0.59$ eV [(a),(c)], and $V=10$ eV, $t_{\text{eff}}= 0.35$ eV, $\Delta_{\text{eff}}= 0.93$ eV [(b),(d)]. The insets show the integrated spectral weight represented in terms of kinetic energy versus photon energy.

FIG. 10. Band structures[(a)] and optical conductivities[(b)] for exact K-P model[Eq. (56)] with $\lambda_1 = -4$, $\lambda_2 = -5$ (solid line) and for the best tight binding fit(dotted line), $t_{\text{eff}}=1.33$, $\Delta_{\text{eff}}=0.6$. The inset shows the integrated spectral weight represented in terms of kinetic energy versus photon energy.

TABLES

TABLE I. Total spectral weight for $t_0=0.622$ eV without Coulomb interaction($U=0$), expressed in terms of K_x and K_z .

$2J_{\text{H}}S_{\text{c}}(\text{eV})$	$\lambda(\text{eV}/\text{\AA})$	$K_x^{0K}(\text{eV})$	$K_z^{0K}(\text{eV})$	$K_x^{300K}(\text{eV})$	$K_z^{300K}(\text{eV})$
2.10	1.38	0.295	0.242	0.290	0.211
2.10	2.20	0.236	0.206	0.248	0.179
2.10	2.90	0.196	0.184	0.219	0.155
2.47	1.38	0.294	0.217	0.277	0.199
2.47	2.20	0.235	0.185	0.236	0.167
2.47	2.90	0.195	0.165	0.207	0.144

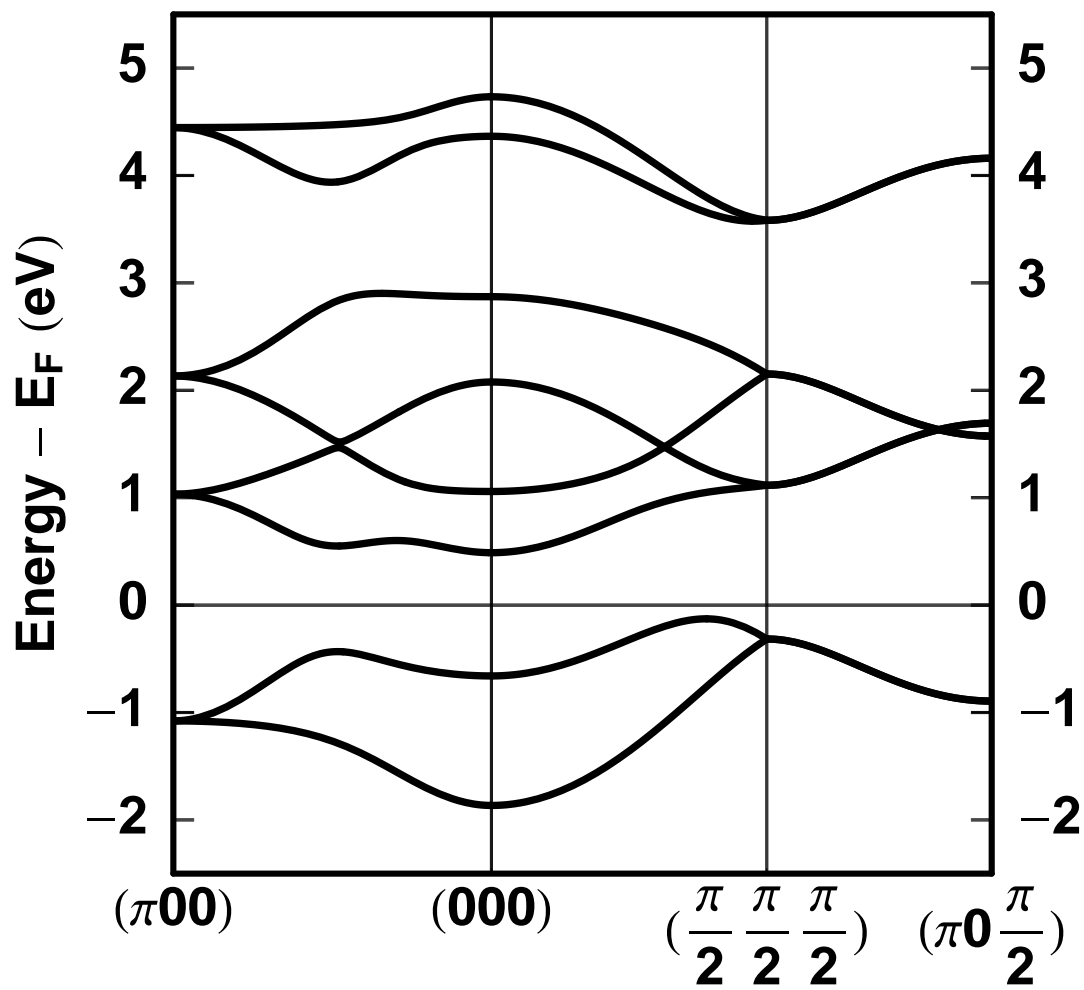


Figure 1, Ahn et. al

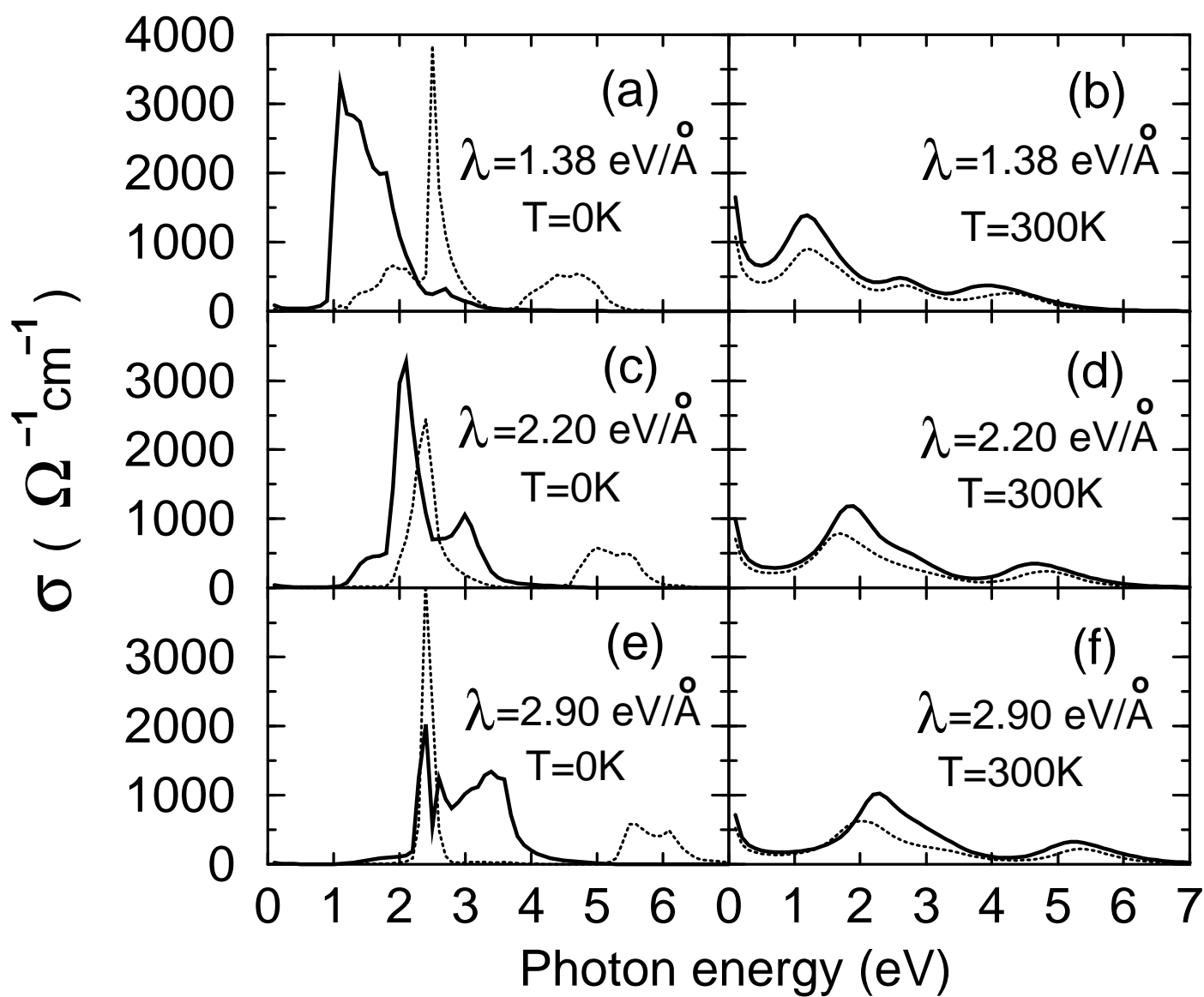


Figure 2, Ahn et. al

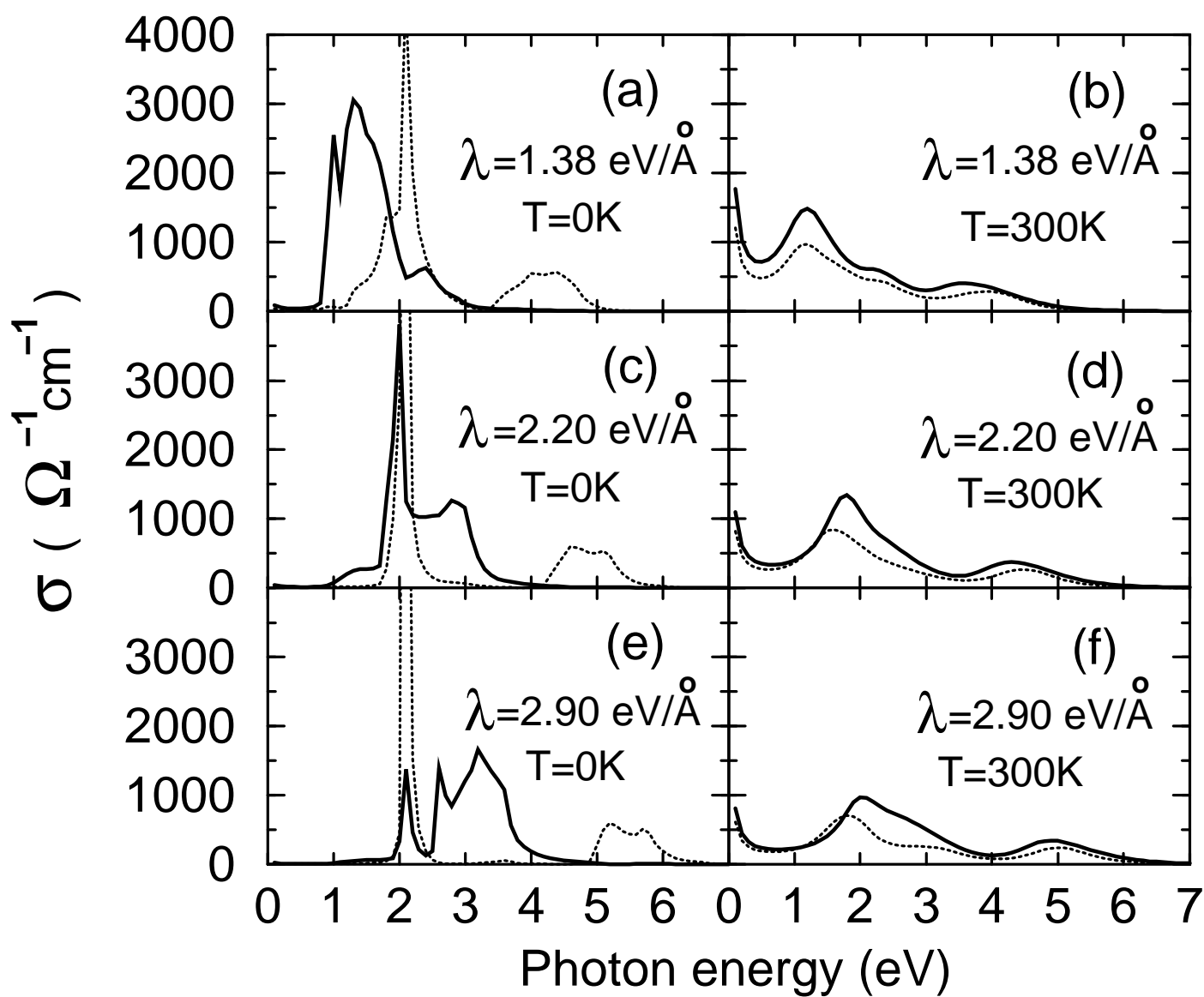


Figure 3, Ahn et. al

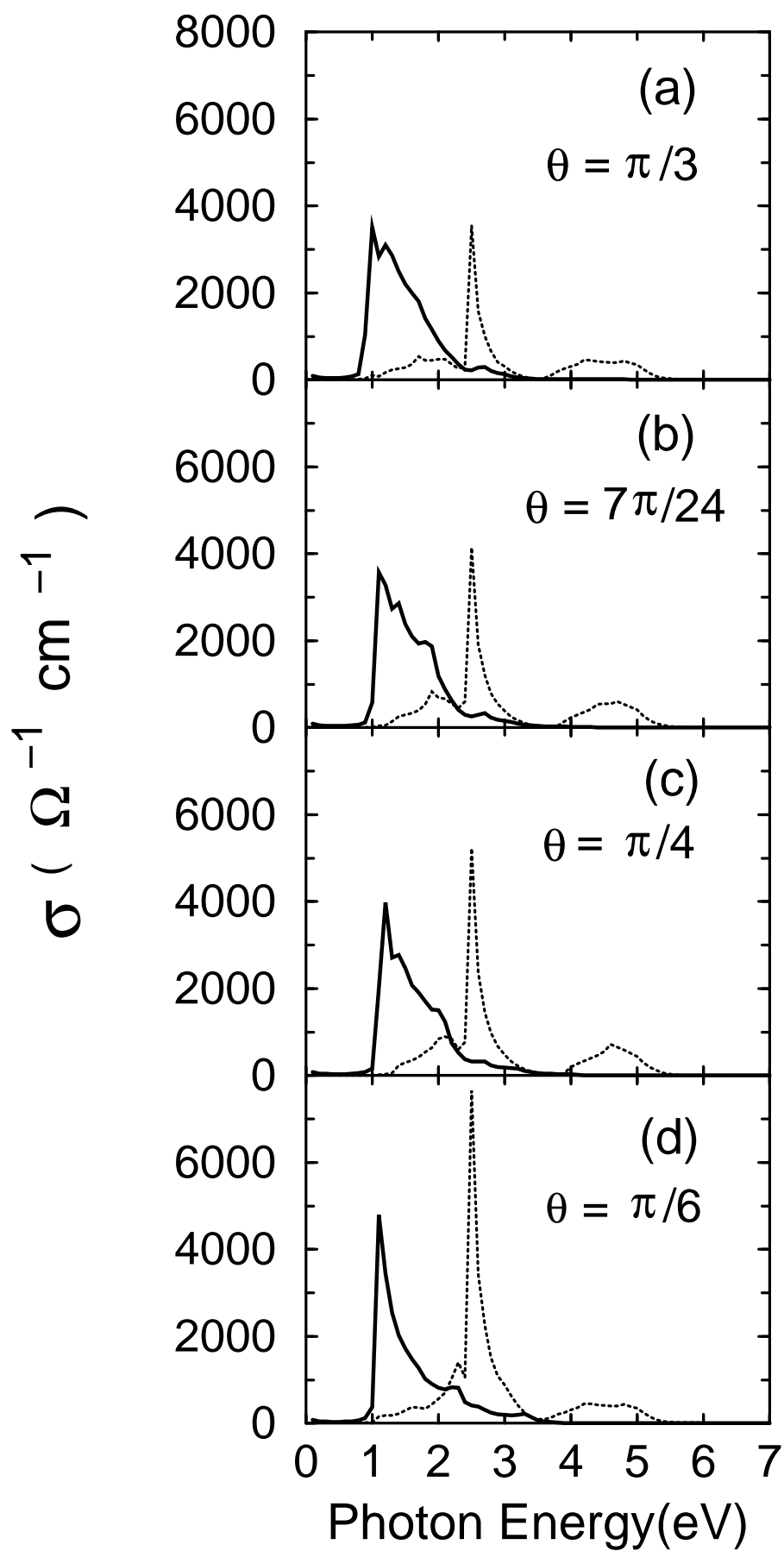


Fig. 4, K. Ahn et al.

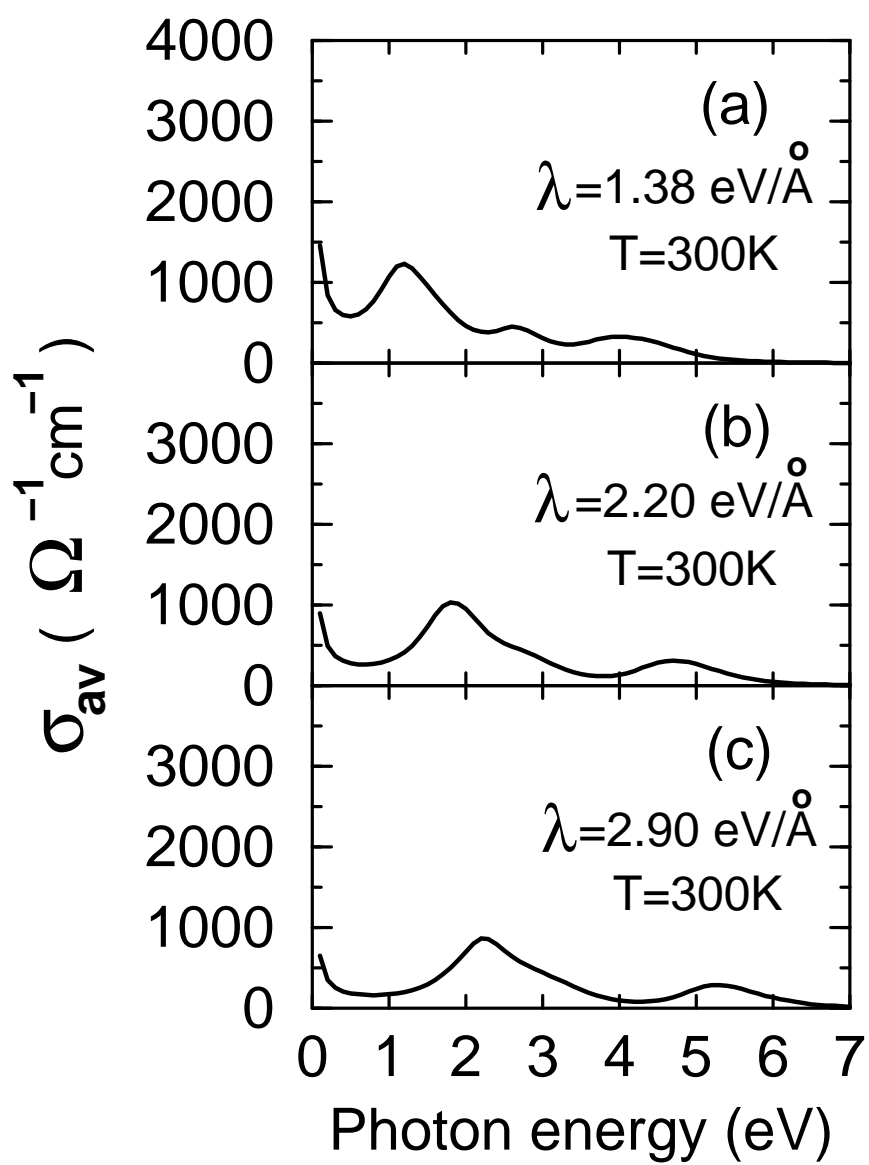


Fig. 5, Ahn et. al

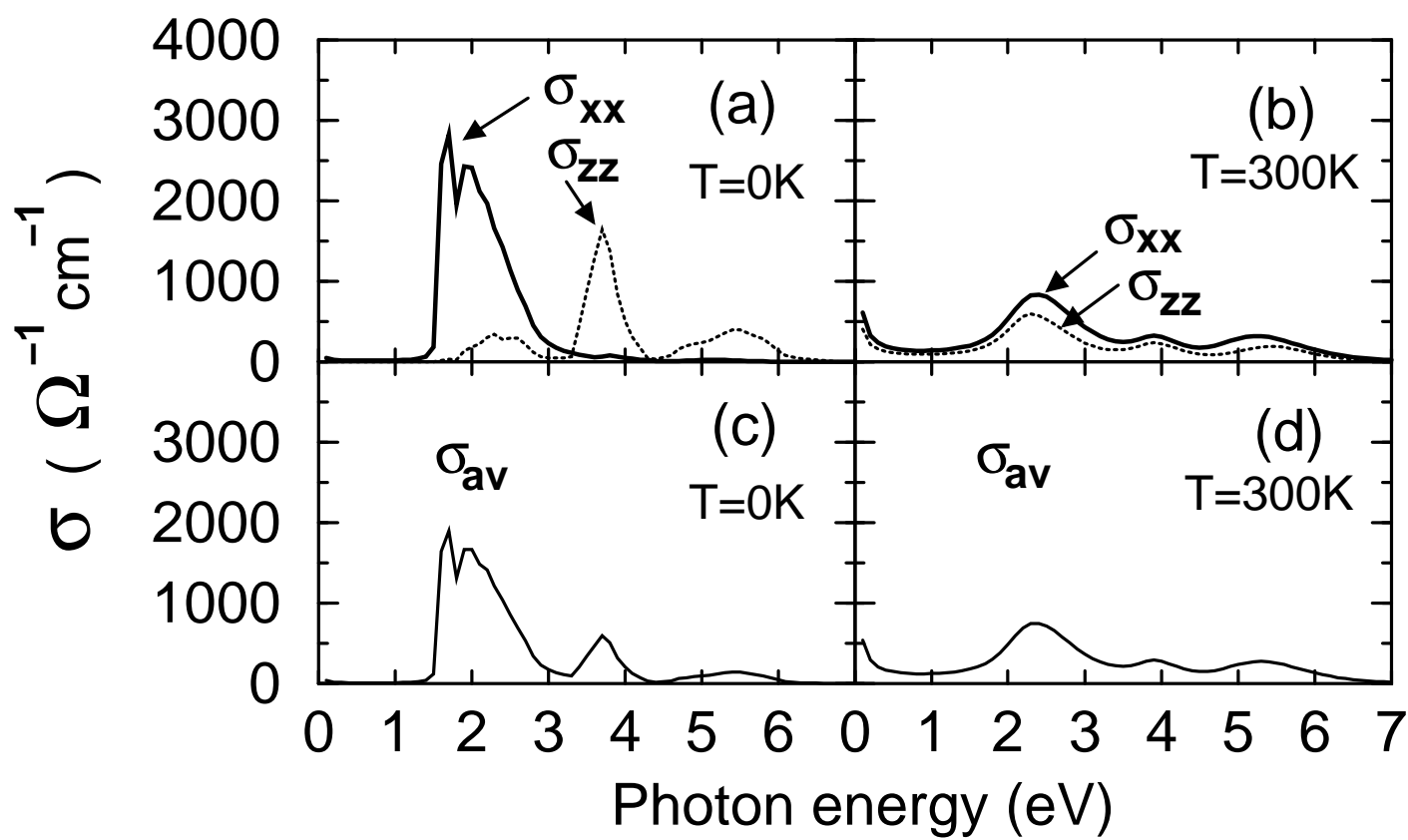


Figure 6, Ahn et. al

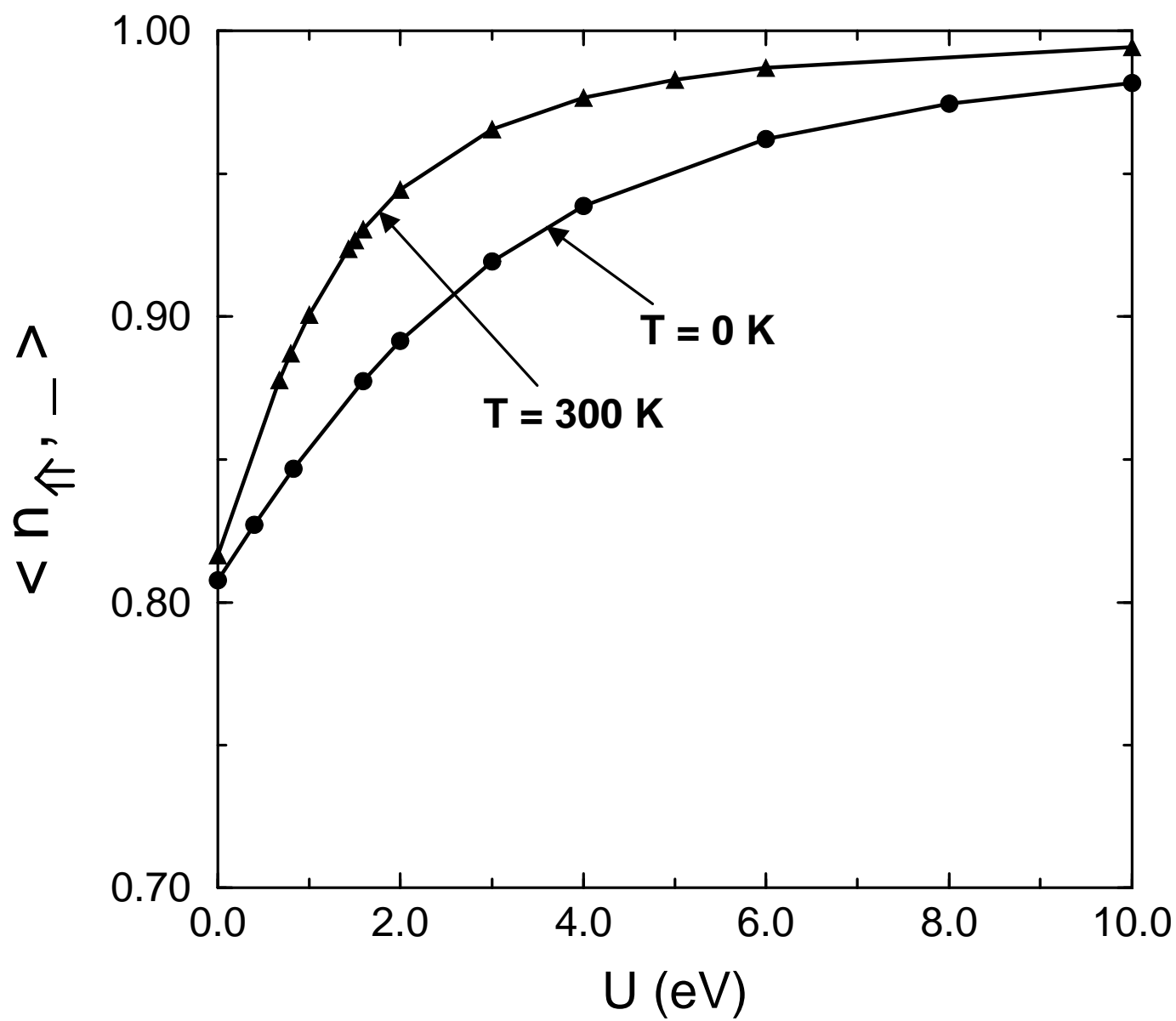


Figure 7, Ahn et. al

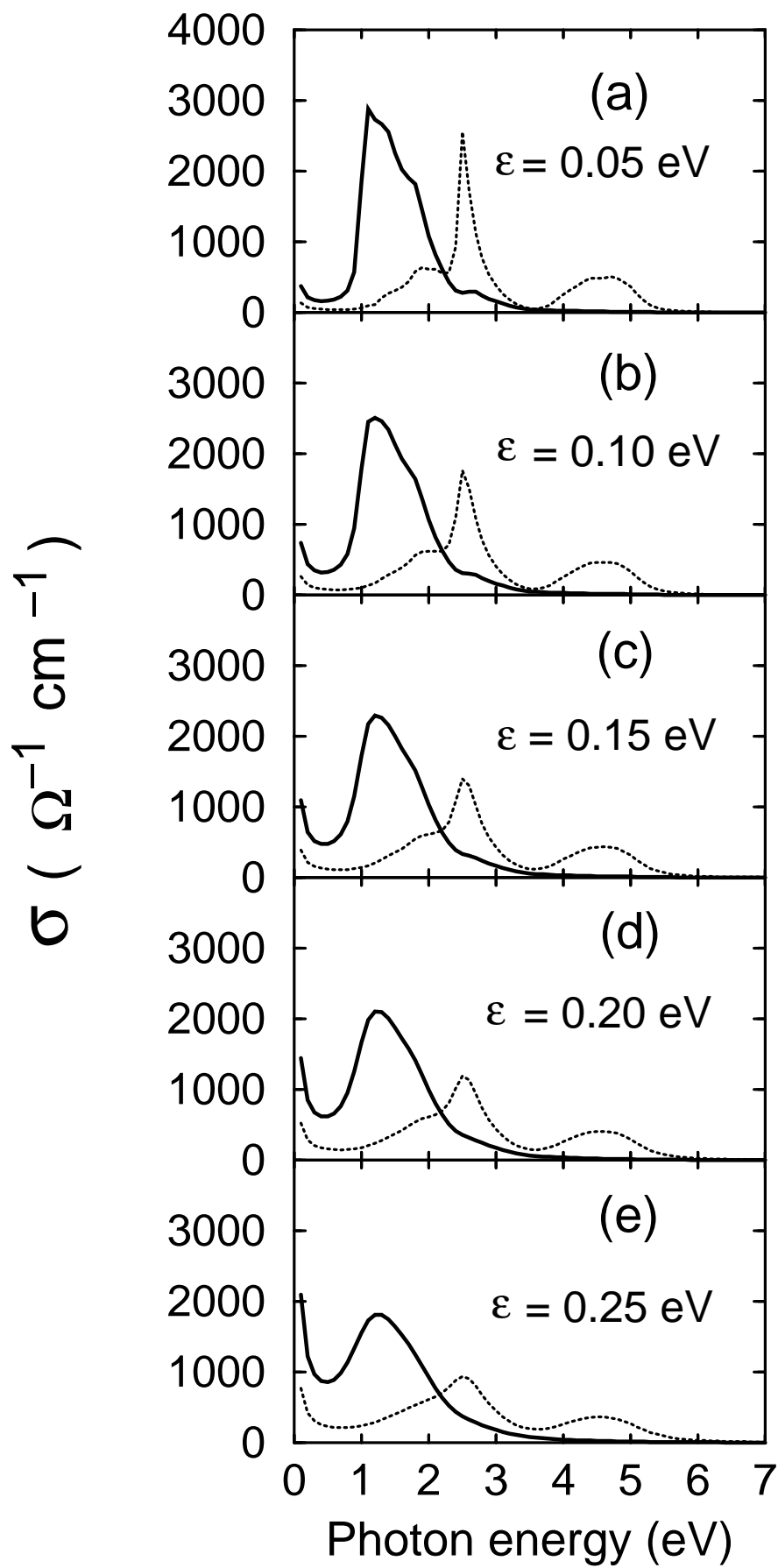


Figure 8, K. Ahn et al.

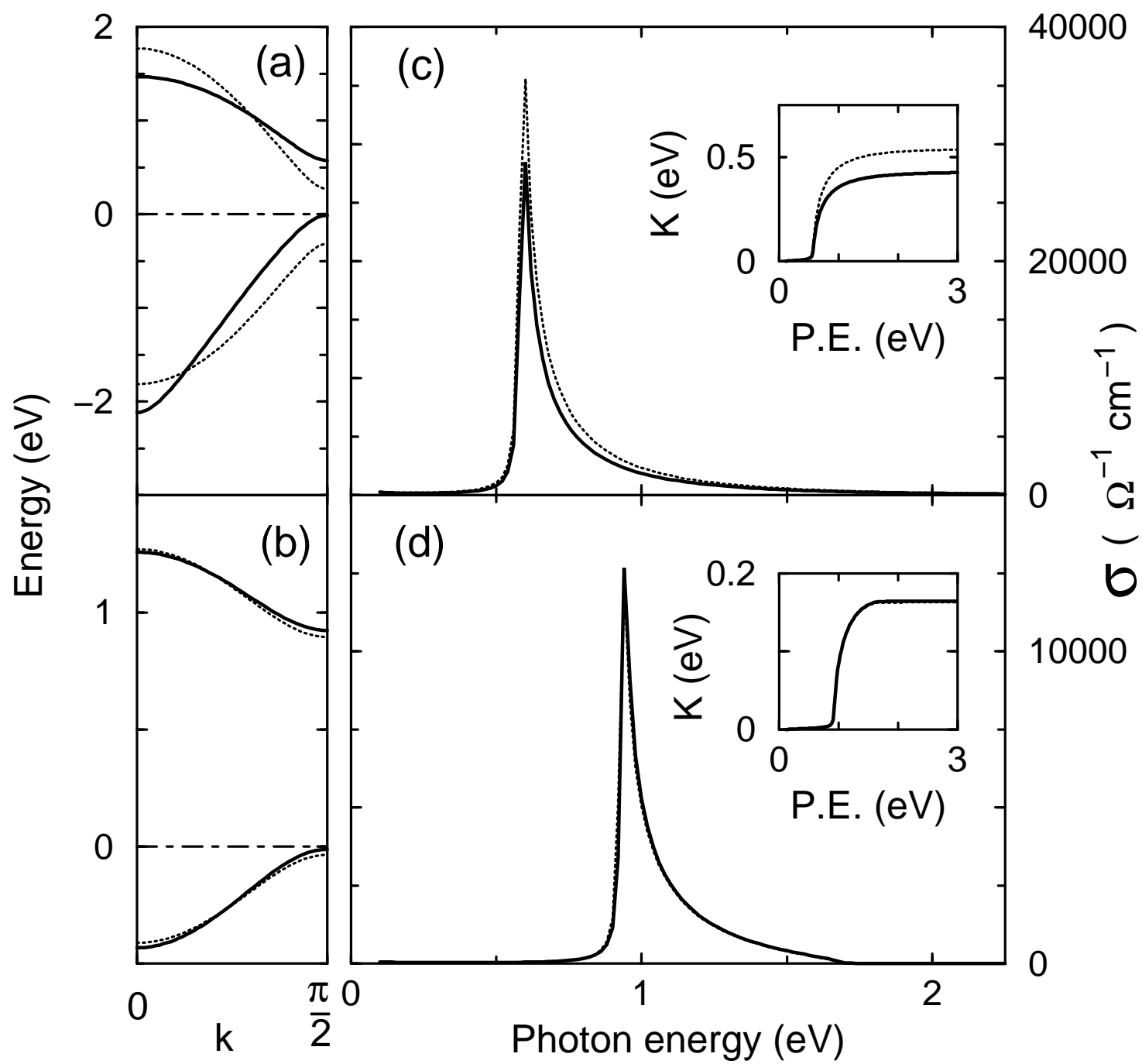


Figure 9, Ahn et al.

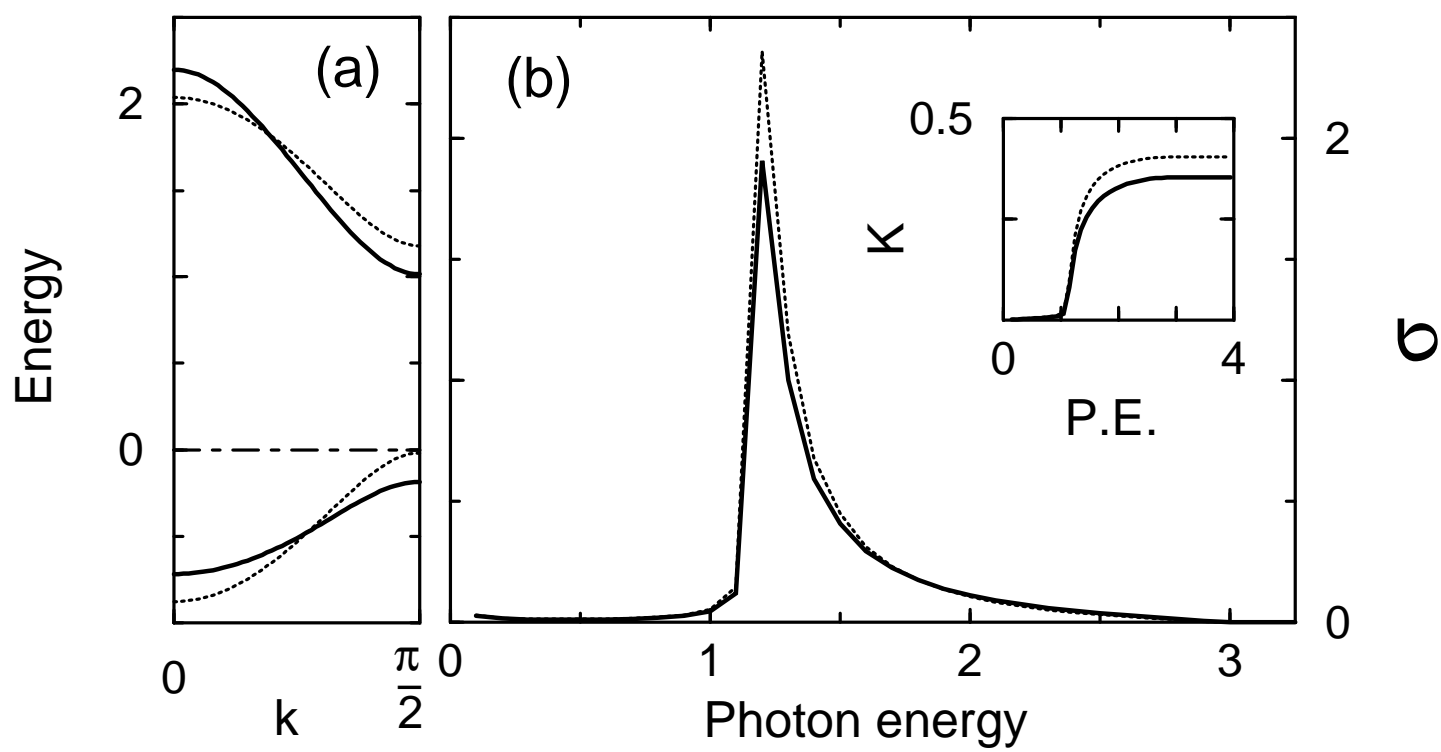


Figure 10, Ahn et al.